Final Report WY-22004F Phase 2

Field Testing and Long-Term Monitoring of Selected High-Mast Lighting Towers (Phase 2)

Jason B. Lloyd, PhD, PE
Jason B. Lloyd & Associates, LLC
760 N. Meaghan Place, Boise, ID 83712
Phone: (860) 941-4668, jasonblloydassociates@gmail.com

Robert J. Connor, PhD, PE
Lyles School of Civil Engineering, Purdue University
550 Stadium Mall Dr., West Lafayette, IN 47907
Phone: (765) 496-8272, rconnor@purdue.edu

Notice

This document is disseminated under the sponsorship of the Wyoming Department of Transportation (WYDOT) in the interest of information exchange. WYDOT assumes no liability for the use of the information contained in this document.

The content of this report reflects the views of the author(s) who are responsible for the facts and accuracy of the data presented herein. The content does not necessarily reflect the official views or policies of WYDOT. This report does not constitute a standard, specification, or regulation.

The State of Wyoming does not endorse products or manufacturers. Trademarks or manufacturers' names appear in this report only because they are considered essential to the objectives of the document.

Quality Assurance Statement

WYDOT provides high-quality information to serve state, industry, and the public in a manner that promotes public understanding. Standards and policies are used to ensure and maximize the quality, objectivity, utility, and integrity of its information. WYDOT periodically reviews quality issues and adjusts its programs and processes to ensure continuous quality improvement.

Copyright

No copyrighted material, except that which falls under the "fair use" clause, may be incorporated into a report without permission from the copyright owner, if the copyright owner requires such. Prior use of the material in a WYDOT or governmental publication does not necessarily constitute permission to use it in a later publication.

- Courtesy – Acknowledgment or credit will be given by footnote, bibliographic reference, or a statement in the text for use of material contributed or assistance provided, even when a copyright notice is not applicable.
- Caveat for Unpublished Work – Some material may be protected under common law or equity even though no copyright notice is displayed on the material. Credit will be given and permission will be obtained as appropriate.

Proprietary Information – To avoid restrictions on the availability of reports, proprietary information will not be included in reports, unless it is critical to the understanding of a report and prior approval is received from WYDOT. Reports containing such proprietary information will contain a statement on the Technical Report Documentation Page restricting availability of the report.

Creative Commons

1. Report No. WY-2004F Phase 2	2. Government Accession No.	3. Recipient's Catalog No.
4. Field Testing and Long-Term Monitoring of Selected High-Mast Lighting Towers (Phase 2)		5. Report Date February 2023
		6. Performing Organization Code:
7. Author(s) Jason B. Lloyd, PhD, PE, 0000-0001-8792-3278 Robert J. Connor, PhD, PE, 0000-0002-6964-3317		8. Performing Organization Report No.
9. Performing Organization Name and Address Lyles Department of Civil Engineering Purdue University 550 Stadium Mall Drive, West Lafayette, IN 47907		10. Work Unit No.
		11. Contract or Grant No. RS07220
12. Sponsoring Agency Name and Address Wyoming Department of Transportation 5300 Bishop Blvd. Cheyenne, WY 82009-3340 WYDOT Research Center (307) 777-4182		13. Type of Report and Period Final Report
		14. Sponsoring Agency Code
15. Supplementary Notes		

16. Abstract:
Phase 1 field monitoring of four high-mast lighting towers (HMLTs) was previously reported on in March 2020. Due to the rare nature of the large amplitude vibration events, a second phase of monitoring was conducted to continue collecting data and to maximize the potential for recording the rare data. Similar to Phase 1, monitoring, Phase 2 included four HMLTs instrumented with sensors to monitor weather and structural response to wind-induced vibrations. The four HMLTs were in different locales within the state of Wyoming, each site being selected specifically due to a history of failed HMLTs at those locations, or nearby. Several HMLTs have failed in recent years, some catastrophically, within Wyoming, from fatigue crack growth at the base plate-to-tube wall welds. Hence, the motivation for the study. Amateur video and some limited data from previous research both supported the possibility that large-amplitude mode I vibration events could be causing the premature fatigue failures. In some cases, it was surmised that ice or snow accumulation on an HMLT could be contributing to changes in the aerodynamic response to varying wind events. The research team remotely monitored the four HMLTs with wind-based and stress-based triggers recording data of ambient weather conditions and the aerodynamic response of the HMLTs. Phase 1 monitoring confirmed the rarity of the large-amplitude events, but could not confirm the contribution of ice or snow accumulation. Phase 2 monitoring was carried out continuously for an additional 18 months. Identical to Phase 1, Phase 2 instrumentation included an ice sensor, anemometer for wind speed and direction, thermocouple for temperature, and strain gages. In this way, the research team was able to determine what the structural response to the large-amplitude events were and if a build-up of ice could be correlated to its occurrence. Two large-amplitude events were recorded during the period of Phase 2 field monitoring. Extreme stress ranges were observed during both events, reaching peak stresses of about 28.5 ksi (ranges of up to 57 ksi) and lasting a few minutes. The extreme events were found to be relatively rare and unpredictable in terms of when they might occur.

17. Key Words High mast lighting tower, fatigue, vibration, wind, lock-in, Wyoming	18. Distribution Statement No restrictions. This document is available through the National Transportation Library and the Wyoming State Library.

19. Security Classif. (of this report) Unclassified	20. Security Classif. (of this page) Unclassified	21. No. of Pages	22. Price

SI* (MODERN METRIC) CONVERSION FACTORS

APPROXIMATE CONVERSIONS TO SI UNITS

Symbol	When You Know	Multiply By	To Find	Symbol
		LENGTH		
in	inches	25.4	millimeters	mm
ft	feet	0.305	meters	m
yd	yards	0.914	meters	m
mi	miles	1.61	kilometers	km
		AREA		
in^2	square inches	645.2	square millimeters	mm^2
ft^2	square feet	0.093	square meters	m^2
yd^2	square yard	0.836	square meters	m^2
ac	acres	0.405	hectares	ha
mi^2	square miles	2.59	square kilometers	km^2
		VOLUME		
fl oz	fluid ounces	29.57	milliliters	mL
gal	gallons	3.785	liters	L
ft^3	cubic feet	0.028	cubic meters	m^3
yd^3	cubic yards	0.765	cubic meters	m^3
		NOTE: volumes greater than 1000 L shall be shown in m^3		
		MASS		
oz	ounces	28.35	grams	g
lb	pounds	0.454	kilograms	kg
T	short tons (2000 lb)	0.907	megagrams (or "metric ton")	Mg (or "t")
		TEMPERATURE (exact degrees)		
°F	Fahrenheit	5 (F-32)/9 or (F-32)/1.8	Celsius	°C
		ILLUMINATION		
fc	foot-candles	10.76	lux	lx
fl	foot-Lamberts	3.426	$candela/m^2$	cd/m^2
		FORCE and PRESSURE or STRESS		
lbf	poundforce	4.45	newtons	N
lbf/in^2	poundforce per square inch	6.89	kilopascals	kPa

APPROXIMATE CONVERSIONS FROM SI UNITS

Symbol	When You Know	Multiply By	To Find	Symbol
		LENGTH		
mm	millimeters	0.039	inches	in
m	meters	3.28	feet	ft
m	meters	1.09	yards	yd
km	kilometers	0.621	miles	mi
		AREA		
mm^2	square millimeters	0.0016	square inches	in^2
m^2	square meters	10.764	square feet	ft^2
m^2	square meters	1.195	square yards	yd^2
ha	hectares	2.47	acres	ac
km^2	square kilometers	0.386	square miles	mi^2
		VOLUME		
mL	milliliters	0.034	fluid ounces	fl oz
L	liters	0.264	gallons	gal
m^3	cubic meters	35.314	cubic feet	ft^3
m^3	cubic meters	1.307	cubic yards	yd^3
		MASS		
g	grams	0.035	ounces	oz
kg	kilograms	2.202	pounds	lb
Mg (or "t")	megagrams (or "metric ton")	1.103	short tons (2000 lb)	T
		TEMPERATURE (exact degrees)		
°C	Celsius	1.8C+32	Fahrenheit	°F
		ILLUMINATION		
lx	lux	0.0929	foot-candles	fc
cd/m^2	$candela/m^2$	0.2919	foot-Lamberts	fl
		FORCE and PRESSURE or STRESS		
N	newtons	0.225	poundforce	lbf
kPa	kilopascals	0.145	poundforce per square inch	lbf/in^2

TABLE OF CONTENTS

LIST OF FIGURES

LIST OF TABLES

LIST OF EQUATIONS

EXECUTIVE SUMMARY

Four high-mast lighting towers (HMLTs) were instrumented with sensors and remote data acquisition systems to monitor weather and structural response to wind-induced vibrations. During Phase 1 of field monitoring, which occurred between 2017 and 2000, the four HMLTs were chosen in different locales within the state of Wyoming, each site being selected specifically due to a history of failed HMLTs at those locations, or nearby (Lloyd, Connor, & Sherman; 2020). Phase 2 monitoring was performed on the same HMLTs at three of the four locations monitored in Phase 1. However, due to a fatigue crack identified by WYDOT during inspection of the Dwyer Junction HMLT at the end of Phase 1 field monitoring, the HMLT was removed from service and the Research Team moved the monitoring system to an adjacent HMLT co-located at the rest stop, near the entrance with US Highway 26. Several HMLTs have failed in recent years within Wyoming, some catastrophically, from fatigue crack growth at the base plate-to-tube wall welds. Hence, the motivation for the study. Amateur video and some limited data from previous research both supported the possibility that large-amplitude mode I vibration events could be causing the premature fatigue failures. Phase 1 field monitoring was able to capture two such large-amplitude events, along with other notable events. Prior to Phase 1 monitoring, it was theorized that ice accumulation on an HMLT could be contributing to changes in the aerodynamic response to random wind events. However, it was found that the presence of ice did not necessarily correlate to the large amplitude vibration events. In other words, it was found that large amplitude events can still occur in warm weather. As done previously, the research team remotely monitored the four HMLTs with wind-based and stress-based triggers programmed into the data acquisition systems recording data of ambient weather conditions and the aerodynamic response of the HMLTs. The monitoring was carried out continuously during Phase 2 for about 18 months. The instrumentation included an ice sensor capable of detecting the presence of ice, an anemometer for wind speed and direction, a surface-mounted thermocouple for temperature of the HMLT, and strain gages for strain (and stress in the pole through a simple mathematic conversion) and stress-range histogram data. This way the research team would be able to determine what the structural response to the large-amplitude events were and if the build-up of ice could be correlated to its occurrence.

Two large-amplitude events and a few notable events were observed during the second phase of field monitoring. Large stress ranges were recorded during the two large-amplitude events, reaching peak stresses of up to about 28.5 ksi (ranges of up to 57 ksi) and lasting several minutes. Once again, the extreme events were found to be relatively rare and unpredictable in terms of when they might occur. Ice accumulation was not correlated to either event. However, snow accumulation was observed on the HMLTs and recorded on video by a WYDOT employee during the March 2022 event at Dwyer Junction making it possible that it contributed to the structural response. Recall that during Phase 1 field monitoring, it was found that the large-amplitude vibrations could occur with or without ice present, suggesting that it is the random resonant pairing of HMLT aerodynamic properties and characteristics of the wind that caused such extreme structural response. This same observation was noted during Phase 2 field monitoring.

CHAPTER 1. BACKGROUND

PROBLEM STATEMENT & MOTIVATION

Wyoming Department of Transportation (WYDOT) has experienced multiple fatigue failures of HMLTs in recent years, some as early as two to three years into the service life of the tower. On occasion, these fatigue failures have resulted in catastrophic collapse. Climate data, such as wind, temperature, and presence of moisture recorded at weather stations in relatively nearby locations, was reported to suggest that there could have been ice or snow accumulation on the towers at the time of the fatigue failures potentially changing the aerodynamic response of the towers. Several amateur videos have also been circulated on the internet displaying extreme amplitude, low-frequency oscillation of HMLTs in several states, typically captured by passing motorists, some of which appeared to occur in warmer temperature where ice could not have played a factor. An additional video was captured by a WYDOT employee toward the end of the Phase 2 field monitoring period in which snow accumulation was visible on the HMLT. Ice was not reported by the monitoring system at that time. However, the effect of ice or snow buildup could not be ruled out, and the accumulation of empirical evidence supported the idea that ice or snow accumulation on the towers could be changing aerodynamic response and contributing to vortex shedding-induced resonance. Previous research by others suggested that very large stress ranges can occur at the tube wall to base plate weld, particularly if in addition to large amplitude vibrations the anchor nuts are not tightened properly. Due to the cubed root relationship of stress range to fatigue loading cycles, it stood to reason that this was a possible factor in the premature fatigue failures.

This report presents the findings and conclusions of the continued field-monitoring project for an additional 18 months aimed at capturing the rare loading event of large-amplitude mode I vibration of 120-ft tall high-mast lighting towers in Wyoming.

OBJECTIVES

The primary objective of the present research was to record data for large-amplitude mode I vibrations of high-mast lighting towers induced by natural wind events. The challenge with this objective is that the events are rare, random and unpredictable. A secondary and related objective was to determine if there was any further correlation between an accumulation of ice or snow on the HMLT and the occurrences; meaning were the large-amplitude lock-in events more likely to occur when there was ice built up on the HMLT. As previously mentioned, this was not always observed during Phase 1 monitoring, but remained an objective of interest for Phase 2. Thirdly, this study set out to add to the understanding of HMLT structural behavior during such events, most importantly the stress ranges at the base plate-to-tube wall welds resulting from large-amplitude displacements. The Phase 2 field monitoring was simply a continuation of the data collection performed during Phase 1, previously reported on (Lloyd *et al*., 2020). Data sets such as this are invaluable for calibration of analytical models for parametric study or for scaled wind-tunnel research. Such engineering-based studies can provide pragmatic solutions to counter or eliminate resonance and improver serviceability of HMLTs.

LITERATURE REVIEW

Connor, R. J., Collicott, S. H., DeSchepper, A. M., Sherman, R. J., & Ocampo, J. A. (2012)

The primary objective of NCHPR Project 10-74 was to improve the reliability of HMLTs. The approach included developing loading and analysis criteria for use in the fatigue design of HMLTs, developing a design methodology and specifications with associated commentary for design of HMLTs, and preparing recommended revisions to the existing AASHTO *Standard Specifications for Structural Supports for Highway Signs, Luminaries, and Traffic Signals*. The research is detailed in NCHRP Report 718 and summarized in Sherman and Connor (2019).

To accomplish the abovementioned objectives, the researchers performed long-term field monitoring on 11 HMLTs ranging in height of 100 to 160 ft. with taper rate of 0.14 incher per ft. They pluck tested an additional 15 HMLTs for dynamical properties. All poles included in long-term monitoring were multi-sided with exception of one circular pole. The poles were monitored over the course of two years. Wind speed data and stress-range histogram data were compiled for each location, forming the basis for the proposed fatigue design loads. In addition, Connor et al. (2012) developed recommended damping ratios for mode I, mode II, and mode III vibration, and determined that mitigation of vortex shedding using double-wrap rope strake reduces the number of accumulated cycles without affecting the effective stress range. They also determined that while infinite life design is appropriate, the lifetime loading cycles for HMLTs exceeds the limiting number of cycles at the constant-amplitude fatigue limit state for the most common fatigue detail (Category E) located at the pole-base plate weld. Additionally, they developed static pressure range values for fatigue evaluation of HMLTs, recommended stress range cycle frequencies for fatigue evaluation of HMLTs, and finally concluded that poles with a vertex toward the prevailing wind are more prone to "lock-in". Lock-in is the term that describes the phenomenon in which the vortex shedding frequency and the structural natural frequency lock-in with one another resulting in large across-wind vibrations.

During the research, a video surfaced on the web showing large amplitude oscillations of a HMLT outside Watertown, SD. The HMLT was not being monitored, so no data were available for the event and it was reported that the pole was removed from service following the event due to cracking. It appeared to have occurred during a late winter storm. This motivated the researchers to comb their data looking for similar events that might have been captured for monitored poles. They found two incidents, one at Creston Junction, WY, and the other at Rapid City, SD. Both cases experienced sustained mode I oscillations of around 10 ksi stress range with sustained winds of about 30 mph. The tower displacements were reported as across-wind.

Magenes, L. (2011)

Magenes (2011) performed the field-testing phase of the three-part study funded by TxDOT with the objective to correlate wind speed and direction to stress ranges in the tube wall to better understand their fatigue performance. Several poles around Texas were instrumented, with size ranges approximating the HMLTs instrumented for the current research within Wyoming.

This study concluded that vortex shedding occurs at a wind speed close to 7 mph, exciting the second natural mode of vibration – noting that the Texas HMLT has a higher taper rate than most poles helping to reduce vortex shedding. This study further concluded that the effective fatigue stress range (or the equivalent constant amplitude stress range) for all locations studied was close to 1 ksi, noting that both vortex shedding and buffeting contributed to fatigue damage of the pole-base plate connection detail.

CHAPTER 2. RESEARCH APPROACH

FIELD MONITORING PROGRAM

Four high mast lighting towers located in different areas of Wyoming were selected by WYDOT for instrumentation and long-term monitoring. The towers were selected from locations of interest to WYDOT, including areas where previous towers had failed in fatigue prior to this research project. The four locations and the characteristics of each tower are discussed below in detail.

During the week of September 28, 2020, researchers from the Steel Bridge Research, Inspection, Training, and Engineering (S-BRITE) Center, at Purdue University, visited each site to clean equipment, update firmware, replace faulty sensors, and perform overall system operational checks. The Research Team also instrumented the fourth tower located at Dwyer Junction in the week of September 28, 2020. Details of the field monitoring are discussed in the following, including the instrumentation, sensors, data acquisition, remote communications, and data storage. Typically, field-testing and fatigue evaluation of structures subject to environmental loads, such as wind, should be tested for a minimum of one year in order to capture all seasonal effects resulting from variable weather patterns. Field-testing for this project continued for about 18 months, finishing in March 2022. It was a continuation of the first phase of monitoring, which was for a two-year period. The first phase of field monitoring was previously reported on and covered the periods of September 2017 to October 2019. The additional months of monitoring performed for this study were an extended effort to capture the relatively rare loading events that cause large-amplitude mode I oscillations of the lighting towers.

Overview of Test Sites

All four HMLTs were instrumented in September of 2019 during Phase 1 testing. During the week of September 28, 2020, each site was visited by the Research Team as part of Phase 2 field monitoring to perform maintenance on the monitoring systems and ensure optimal performance. Dysfunctional strain gages were replaced, weather protections were replaced, modems were replaced with new models, and data loggers were updated and cleaned. All systems were checked for proper function before the Research Team left each site. Details of the sensor installation are discussed in the next section, entitled *Instrumentation*. The four locations of the towers were the Vedauwoo Interchange (District 1), Dwyer Junction (District 2), Baxter Interchange (District 3), and Buffalo Tri-Level (District 4).

Vedauwoo Interchange:

The HMLT monitored in District 1 was positioned on the east side of Interstate 80 at the Vedauwoo exit (Exit 329). Figure 1 shows an image taken from Google Earth where the Vedauwoo climbing area access road can be seen intersecting with I-80. The red arrow indicates the location of the HMLT just south of the exit. Figure 2 shows the HMLT from the roadway driving westbound along I-80. The image shows the orange equipment box, which housed the data acquisition system (DAQ), and the temporary pole on which the anemometer and ice sensor

were installed. The temporary pole was installed by WYDOT a minimum of 10 ft. from the HMLT to ensure wind measurements were not affected by proximity of the pole.

Adapted from an Original Photo: ©2019 Google®

Figure 1. Photo. Location of HMLT tested at the Vedauwoo Interchange.

Original Photo: ©2019 Google®

Figure 2. Photo. Westbound street view of the HMLT at Vedauwoo Interchange.

Dwyer Junction:

The HMLT monitored in District 2 is positioned at the Dwyer Junction rest stop adjacent to the entrance off US Highway 26 leading to the truck parking area. Figure 3 shows an image taken from Google Earth where the Junction of I-25 and U.S. 26 can be seen. The red arrow indicates the location of the HMLT within the rest stop area. Figure 4 shows the HMLT from the roadway driving into the rest stop area. The image shows the orange equipment box that housed the DAQ, and the temporary pole on which the anemometer and ice sensor were installed.

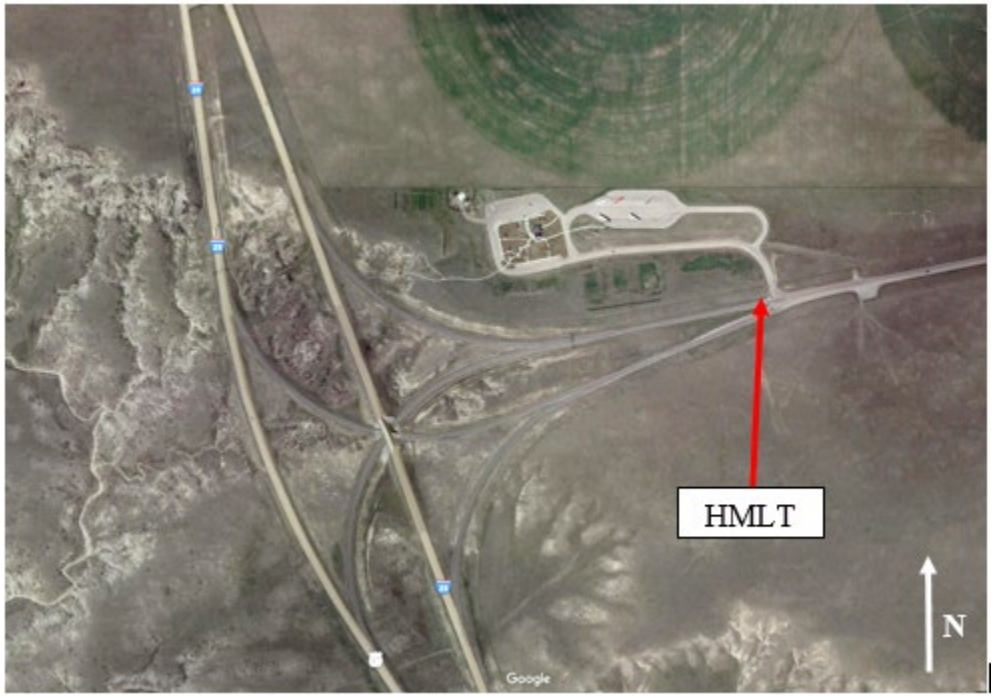

Adapted from an Original Photo: ©2019 Google®

Figure 3. Photo. Location of HMLT tested at Dwyer Junction.

Original Photo: ©2022 Google®

Figure 4. Photo. Street view of the HMLT at Dwyer Junction, looking west.

Baxter Interchange:

The HMLT monitored in District 3 is positioned in the median of Interstate 80 at the Baxter Interchange (Exit 111). Figure 5 shows an image taken from Google Earth where WYO-370 can be seen intersecting with I-80. The red arrow indicates the location of the HMLT just west of the exit. Figure 6 shows the HMLT from the roadway driving eastbound along I-80. The image shows the orange equipment box, which housed the DAQ, and the temporary pole on which the anemometer and ice sensor were installed.

Adapted from an Original Photo: ©2019 Google®

Figure 5. Photo. Location of HMLT tested near Baxter Interchange.

Original Photo: ©2019 Google®

Figure 6. Photo. Eastbound street view of the HMLT near Baxter Interchange.

Buffalo Tri-Level:

The HMLT monitored in District 4 is positioned in the median just east of the I-25 on-ramp at the Buffalo Tri-Level interchange of I-90 and I-25. Figure 7 shows an image taken from Google Earth where the entire interchange can be seen. The red arrow indicates the location of the HMLT. Figure 8 shows the HMLT from the roadway driving southbound along the I-25 on-ramp. The image shows the orange equipment box, which housed the DAQ), and the temporary pole on which the anemometer and ice sensor were installed.

Adapted from an Original Photo: ©2019 Google®

Figure 7. Photo. Location of HMLT tested at Buffalo Tri-Level.

Original Photo: ©2019 Google®

Figure 8. Photo. Southbound street view of the HMLT at Buffalo Tri-Level.

Summary of HMLT Dimensions and Base Weld Detail

The dimensions characterizing each HMLT are summarized below in **Error! Reference source not found.**. All of the HMLTs shared similar dimensions, with the only exceptions being the base plate thickness and tube base diameter for the Vedauwoo Interchange.

Table 1. Key dimensions for each HMLT

HMLT	Pole Height (ft.)	Tube				Base Plate			Bend Radius-to-Tube Thickness Ratio	Base Plate-to-Tube Thickness Ratio
		Taper (in/ft.)	Base Dia. (in)	Thick (base) (in)	No. of Sides (base)	Plate Dia. (in)	Bolt Circle Dia. (in)	Thick (in)		
Vedauwoo Int.	120	0.14	23.28	0.375	16	35	29	2.0	10.6	5.3
Dwyer Junct.	120	0.14	24.25	0.375	16	36	30	2.5	10.6	6.6
Baxter Int.	120	0.14	24.25	0.375	16	36	30	2.5	10.6	6.6
Buffalo Tri	120	0.14	24.25	0.375	16	36	30	2.5	10.6	6.6

The last two columns are noted as a convenience to the reader to compare to research conclusions reported by Nasouri et al. (2019b). Recall that in this study the authors used finite element analysis to carry out a parametric study to characterize HMLT characteristics and dipping practices that may help reduce the risk of cracking during hot dip galvanizing. The bend

radius-to-tube thickness ratios for these HMLTs monitored as part of this research are toward the high side of the range studied by Nasouri et al., which varied from 3 to 14, with 14 having the most beneficial results. While it cannot be determined with a high level of certainty, this would suggest that the bend radius-to-tube thickness geometry of the Wyoming HMLTs, included in this research should have helped reduce risk of cracking during galvanizing. The base plate-to-tube thickness ratios are approximately mid-range of those studied by Nasouri et al., which ranged from 11 to 2, with 2 having the most beneficial results. Once again, it is difficult to draw a conclusion from this, but it may suggest that there is moderate risk of galvanizing cracking to this geometric relationship.

The weld detail for the base plate-to-tube wall weld is shown in Figure 9. This detail was typical for all monitored HMLTs, as was confirmed in the fabrication shop drawings for each. This detail is different than the typical TxDOT weld detail that was modeled in Nasouri et al. (2019a) and (2019b). The typical TxDOT weld detail for HMLTs also has a full penetration weld; however, it has an external collar (or ring) left in place with seal weld on the interior of the tube wall. This is pointed out only to ensure the reader is aware that while some conclusions from Nasouri et al. (2019a) and (2019b) may have applicability, it is difficult to draw absolute conclusions due to the fact that there are minor differences in the welded detail of primary concern.

Finally, the fatigue category of the tube wall-to-base plate weld shown in Figure 9 is E', as provided in AASHTO *Standard Specifications for Structural Supports for Highway Signs, Luminaires, and Traffic Signals*, Article 11.9.

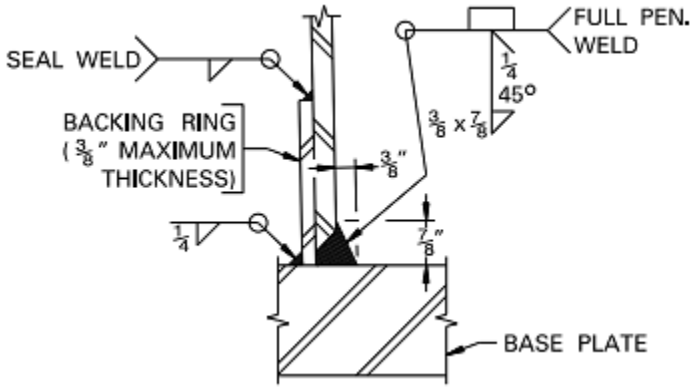

Source: WYDOT Standard Details, Sheet 1 of 3

Figure 9. Base plate-to-tube wall weld detail.

Instrumentation

The Research Team instrumented and checked existing instrumentation for all HMLTs monitored in this study during the week of September 28, 2020. During Phase 1 testing, WYDOT personnel had installed a separate temporary pole at each location for positioning of the anemometer and ice sensor. An example of this is shown in Figure 10. Recall that these poles were all located a minimum of 10' from the HMLT to ensure wind patterns were not interrupted

by proximity to the HMLT. The installation height was within 10percent of industry standard but varied slightly for each anemometer based on the top elevation of the temporary poles. The industry standard for wind measurement is 33 ft. above the ground, as defined by AASHTO *Standard Specifications for Structural Supports for Highway Signs, Luminaires, and Traffic Signals*, Article 3.2, Basic Wind Speed. Slight variance from the standard 33 ft. is not believed to significantly impact the wind data.

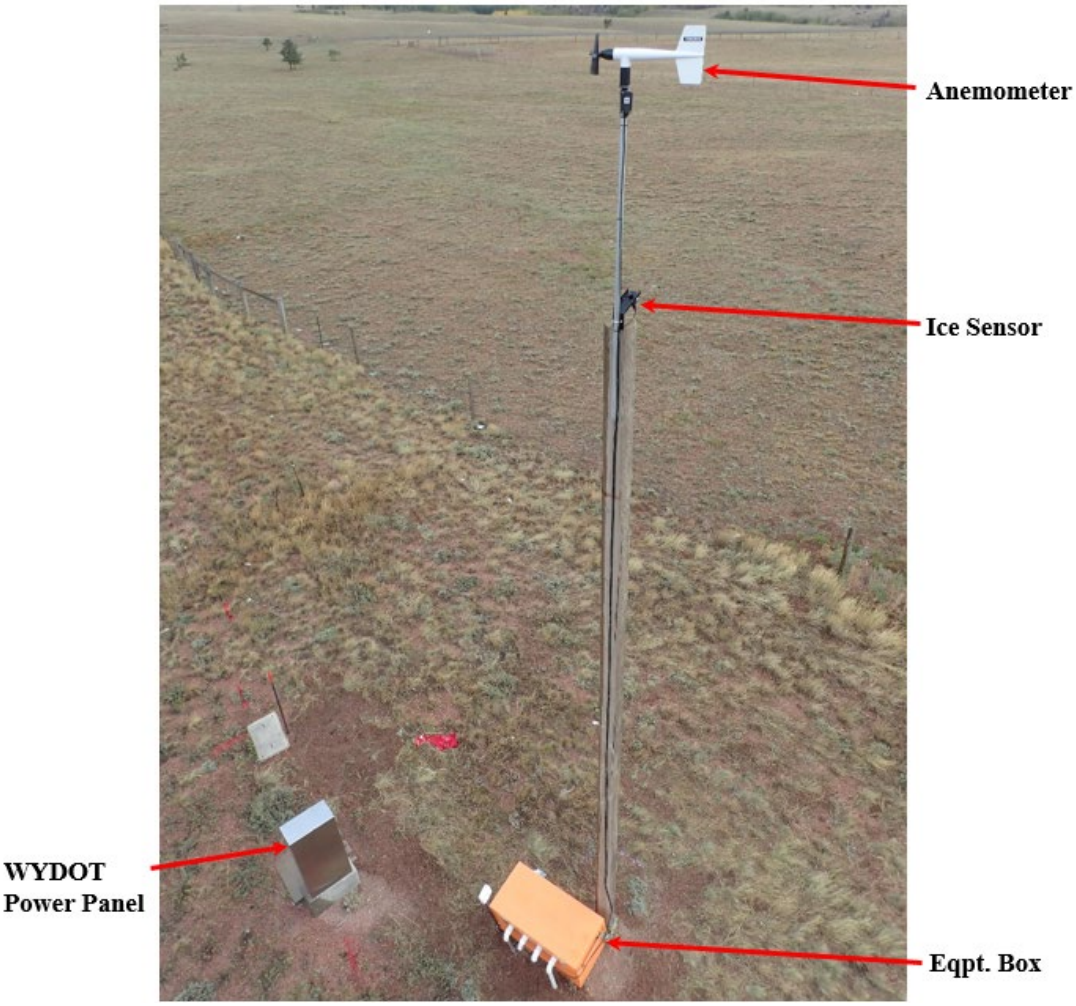

Figure 10. Temporary pole and equipment box

Equipment Box

Extensive measures were taken to protect the equipment during the long-term monitoring enabling safe and reliable operation for the duration of testing. The equipment boxes were made from steel job boxes, modified by the Research Team for the purpose of protecting the monitoring and communications equipment from the environment, theft, and vandalism. An example of one is shown in Figure 11. The boxes were outfitted with two layers of insulation to help moderate interior temperatures. Additionally, the boxes were fitted with a ventilation fan and exhaust duct to circulate interior and exterior air when interior temperatures became too warm. This was monitored and controlled using the CR6 Datalogger.

A shelf was built into the box to set the data logger and modem. Below the shelf the battery bank and charging unit were stored. Wire ports were installed at the front enabling penetration of the box for communications and sensor wires while maintaining a seal against weather and rodent entry. Ports were sealed around the wires and cables. Conduit was installed in approximately 6-in deep trenches between the box, and either the HMLT or anemometer pole to keep wires out of the reach of lawn mowers and rodents. The conduit was brought out of the ground adjacent to the HMLT, as seen in Figure 12. The equipment box was fitted with a gasket around the lid to further seal against dust and moisture intrusion, dual locks to prevent unauthorized access, and each was chained to either the HMLT or anemometer pole. Finally, the Research Team placed ant bait and mothballs inside each box in order to mitigate pest intrusion and sealed the lock ports against rainwater infiltration.

Figure 11. Equipment box

Figure 12. Example of underground conduit used to protect signal wires.

Power Supply

The power supply is shown in Figure 13, which was housed inside the equipment box. The primary power source was local 120VAC power located at the power panel for each HMLT. An extension cord was run underground from the power panel to the interior of the equipment box. The battery charger/maintainer was plugged into the local 120VAC power. A NOCO Genius G15000 12V/24V 15A charger was used. This charger is able to rapidly charge low batteries. It is also equipped with battery maintaining logic allowing it to monitor battery voltage and supply commensurate drip charge to the system, as needed to maintain the battery bank at full charge without overcharging.

Four deep cycle marine batteries were wired in parallel between the battery charger, and the monitoring and communications equipment. The battery bank was wired in parallel making amperage-hours additive to maximize backup power to protect against local power outages or brown-outs and maximize DAQ system time of operation. A terminal board was wired into the battery bank, which distributed the required 12VDC power to all of the monitoring and communications equipment. Excitation voltages required for the operation of the sensors were supplied by the data logger. The exception to this was the ice sensor, which required a 24VDC

power supply to heat the probe tip element and melt any accumulated ice. This power was supplied using a Mean Well HEP-100 AC-DC power supply that was plugged directly into the local 120VAC power cord.

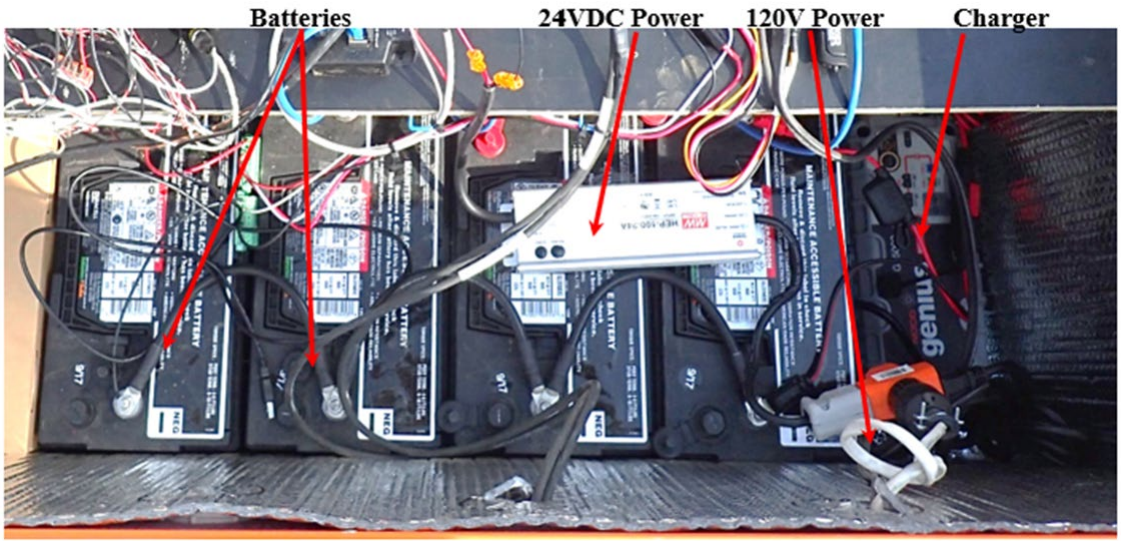

Figure 13. Battery bank power system

Datalogger

The data logger used for long-term monitoring was the Campbell Scientific CR6, as seen in Figure 14. The CR6 is a very low power, versatile 24-bit resolution ADC data logger with programmable universal terminals that can be configured for essentially any sensor. The CR6 has an onboard central processing unit (CPU) allowing programming and stand-alone operation. The CR6 is relatively small, but can be expanded using CDM-A116 input modules with capacity for 16 differential channels each. A CR6 and CDM-A116 were used at each site during field-testing to sample data from several foil resistance strain gages, the anemometer, ice sensor, thermocouple, and accelerometer. In addition to sampling and recording data, the CR6 also communicated via cellular modem with a remote server housed at Purdue University for data storage, as well as monitored the interior temperature of the equipment enclosure triggering the internal ventilation fan when required to moderate operating temperatures for the equipment and battery bank. Finally, the CR6 monitored the voltage of the battery bank as an indicator of battery health and operation. The CR6 was also furnished with a 2 GB Micro SD card for local data storage. All data sampled and recorded by the data logger and expansion module were saved locally to the micro SD card. Upon link-up with the remote server, the data was copied from the micro SD card and transferred to the server. This provided an additional layer of back up for all data. Data collection and storage is further explained below.

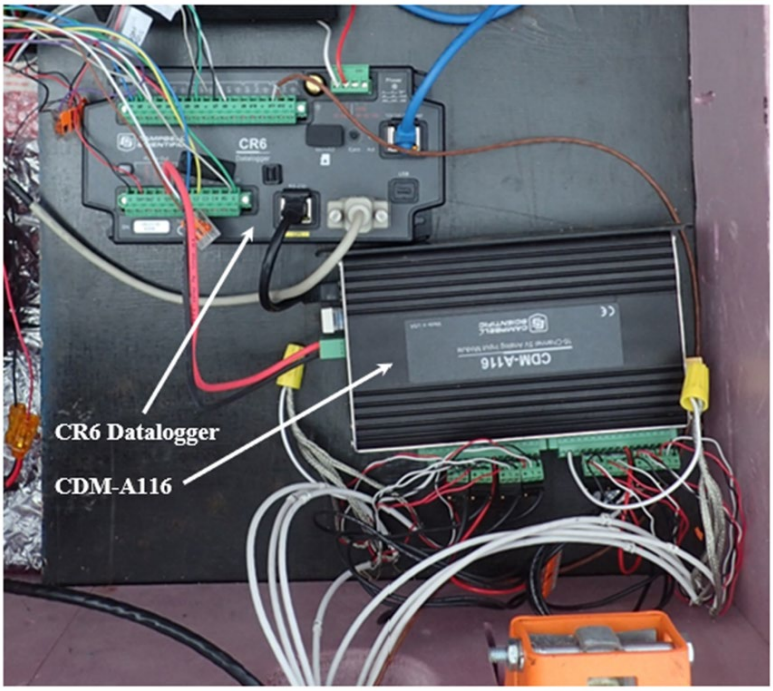

Figure 14. CR6 Datalogger and CDM-A116 Module

Communications

Remote communications with the data logger were achieved via a cellular modem. A couple of the modems purchased new for Phase 1 testing did not survive for Phase 2. Thus, the Research Team replaced two modems, one at the Baxter Interchange and one at the Vedauwoo Interchange, with a Teltonika RUTX11 industrial cellular router/modem. The other two locations remained connected via the original modem, a model CalAmp Fusion Dual Network LTE Router. All four modems were setup with a Verizon Wireless data SIM card and were connected to a Dual LTE/4G Yagi directional antenna. Once the modems and antennas were powered on and locally connected to a laptop, the antenna was rotated until the strongest signal was acquired.

Anemometer

The wind monitor used was the Young Model 5103, as can be seen Figure 15. It is a high performance corrosion-resistant wind speed and direction sensor. The propeller produces an AC sine wave voltage signal whose frequency can be sampled by the data logger and the vane angle (direction of wind) is sensed by a precision potentiometer. Results were returned using a 3-second running average, which is a common averaging time for wind gust measurements, and were converted to speed and angle using calibrated multipliers. All results signify the direction from which the wind is blowing (e.g., 270 degrees would indicate a wind blowing from the west toward the east).

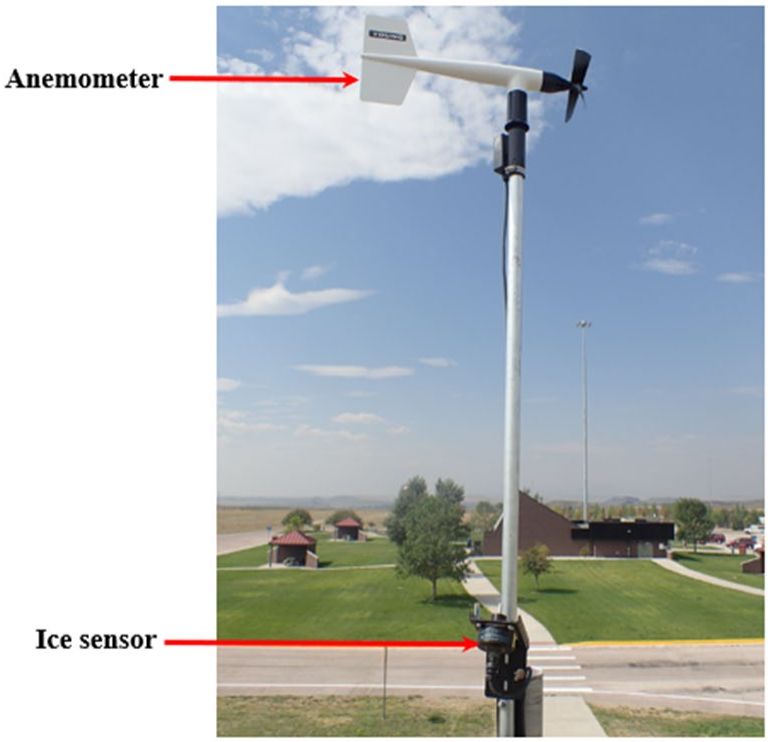

Figure 15. Typical installation of anemometer and ice sensor

Ice Sensor

The freezing rain sensor is made by Rosemount Aerospace, Inc., Model 0871LH1. It detects the presence of icing conditions, or ice accumulation. The installation location can be seen in Figure 15, showing it mounted at the top of the temporary pole, below the anemometer, on the manufacturer-provided mounting bracket. The ice sensor operates using resonant frequencies of a nickel alloy probe. As ice collects on the probe, the added mass causes the resonant frequency to decrease. When the frequency decreases to about 130 Hz (resulting from a layer of ice of about 0.02 inches), the data logger logs an ice event and the ice sensor automatically defrosts the probe and begins the process again. When the pole at Dwyer Junction was removed at the conclusion of Phase 1 field monitoring, the WYDOT removal team decided to cut the cables to the ice sensor. This unfortunately caused internal damage to the electronics of the ice sensor. The Research Team investigated the feasibility of repairing or replacing the sensor, but ultimately the project team from WYDOT decided that it was not worth the expense. Instead, the ice sensor was removed from Baxter Interchange (this site was chosen due to being the least active site for wind events during Phase 1 testing) and relocated to Dwyer Junction on the newly instrumented pole. This proved to be a prudent decision because no wind events were observed at Baxter Interchange and Dwyer Junction continued to be one of the most active sites.

Figure 16. Freezing rain sensor and mounting kit

Strain Gage

Stresses in the tube wall were measured using eight weldable, foil resistance strain gages produced by Vishay Micro-Measurements. The gages were model LWK-06-W250B-350 with an active grid length of 0.25 inches, strain range of ±5000 µin, and nominal resistance of 350 ohms. Excitation voltage was five volts. This type of strain gage is a uni-axial, foil resistance type gage that is temperature compensated for use on structural steel and were wired to the data logger in a three-wire configuration to cancel out lead wire temperature effects. An example of the installation of the weldable strain gage, prior to application of weather protection, is shown in Figure 17.

The strain gage comes pre-bonded to a steel tab from the manufacturer, making installation simpler, more versatile in poor weather, and less prone to mistakes. To attach them to the structure, several pinprick-size resistance spot welds are made on the steel tab. The spot welds pose no short or long-term concern with respect to stress concentration or fatigue. The surface of the steel girder is first prepared by grinding smooth down to base metal and then cleaning with degreaser agent. Next, the gage is spot welded into place, then the exposed base metal is coated with zinc-rich paint, and finally a weather protection system is installed to guard the gage against the environment.

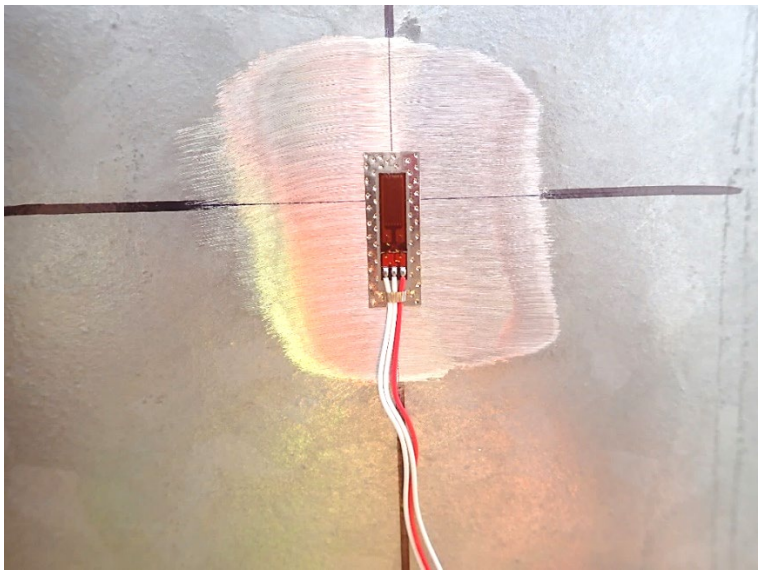

Figure 17. Weldable strain gage

All strain gages were installed seven feet above the top surface of the base plate, providing a distance from the hand hole slightly greater than one and half times the diameter of the HMLT. A single gage was installed on every other tube wall flat, providing nominal stress measurement along all the major axes with a redundant gage for each. Having the measured nominal stress range at a known height on the pole allows the Research Team to validate statics and extrapolate the nominal stresses at the base of the tube near the base plate weld. Figure 18 shows the typical installation of the gages, and Appendix A of Phase 1 report contains the detailed instrumentation plans for each location monitored (Lloyd *et al*., 2020). Channel, or gage, 1 (referred to in data plots as "FG(1) for "foil-resistance gage") was always installed on the flat facing magnetic north.

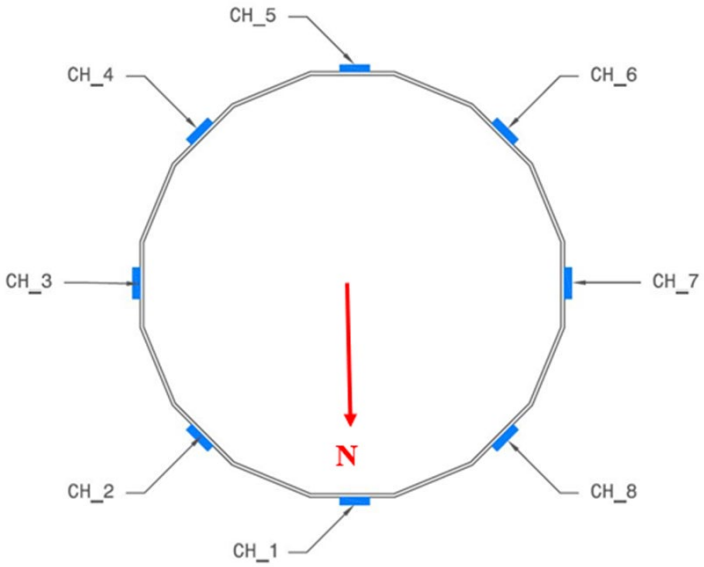

Figure 18. Sketch showing installation of strain gages on tube wall cross-section

Thermocouple

A twisted shielded thermocouple wire produced by Omega, type FF-J-24-TWSH-SLE, was installed on the exterior surface of the HMLT tube wall to collect data on the pole tube wall surface temperature. This data helped correlate with presence of ice data from the freezing rain sensor to validate potential for presence of ice. The surface temperature is also a good set of data to have if needed to understand ambient conditions surrounding the HMLT.

Data Collection and Storage

There were three different primary types of field test data collected and stored throughout the second phase of the project, namely, stress range histogram (using the Rainflow algorithm), ambient data, and triggered time-history data.

Stress Range Histogram Data

Stress range histogram data were collected using the Rainflow algorithm. The Rainflow-counting method is used in the processing and analysis of fatigue data to reduce the highly variable spectrum of stress resulting from random loading sequences into sets, or bins, of equivalent stress cycles. Stress range histograms are generated from stress time-history records, or a continual sampling of data through time. Stress time-history data records quickly become prohibitively large and unmanageable. Thus, the data logger is programmed to buffer the stress time-history data over a period, process it through the Rainflow-counting algorithm generating the histogram, and then discard the buffered data, and begin again. The process captures the equivalent stress cycle history while condensing the information to a manageable amount that can be readily stored and remotely transferred. The period of time over which data were processed into histograms was 10 minutes. This is a typical period used in field testing of bridges and other metal structures and is considered by the authors to provide an accurate, yet conservative, representation of the variable stress spectrum experienced by the structure.

Ambient Data

For the purposes of this research project, ambient data refers to a collection of maximums and averages over a pre-determined period for wind speed, wind direction, steel surface temperature, and battery bank voltage. These data provide a snapshot of ambient temperatures and wind characteristics, along with battery bank health, throughout monitoring, which his particularly useful during periods in which triggered time-history data are not being collected.

Triggered Time-History Data

Triggered time-history data were collected using programmed logic that the data logger used to compare sampled data from the sensors to trigger thresholds. If the data value met the criterion of a trigger event, the data logger would record the buffered time-history data leading up to the trigger event, and then a programmed set of data, typically over a desired period, following the trigger. Once triggered, the data recorded was a continuous time-history intended to record periods of high wind buffeting. Triggers were based on wind speed, as well as peak stress. During the early stages of Phase 1 testing, the wind speed triggers were 30 mph, 40 mph, and 50 mph. Later in the project, after collecting sufficient 30 mph trigger event data, the wind triggers

were limited to the higher wind speeds of 40 and 50 mph. Thus, during Phase 2 testing, only the 40 and 50 mph triggers were utilized. Peak stress triggers were again set at ±5 ksi and ±10 ksi in the event that low wind speed buffeting might cause resonant high amplitude oscillations. In each trigger event, data were recorded into unique tables.

Data Backup and Security

Data collection and storage for long-term monitoring was carefully built with multiple layers of security and backup. As data was collected, it was stored locally on the micro-SD card in the data logger. The card had sufficient capacity for approximately three months of data at the windiest of the four locations. The data was temporarily stored on the micro-SD card in between remote communication linkups with a server at Purdue University. A software produced by Campbell Scientific, Inc., called LoggerNet, was installed on the server. This software has many functions related to data logger support, such as programming, communications, and data retrieval. It has the capacity to manage communications and data retrieval with a network of data loggers simultaneously. It can be used to remotely communicate with a data logger on demand or automatically at a user-defined interval. In this case, LoggerNet was programmed to contact each data logger every 15 minutes and collect all new data since the previous linkup. In the case that remote linkup could not be made at any given interval, the data would remain on the micro-SD card at the data logger until communications could be re-established. Over the course of the 18 months, this occurred occasionally, but not consistently and provided a very reliable communications system. Once the data was retrieved from the data logger it was securely stored on the server. The server was then backed up nightly to backup servers also located at Purdue University. In addition, about every one to two months the data was also manually copied from the primary server by a member of the Research Team and saved to commercially available cloud storage. This means that at any given time the same data could be obtained from three or more servers providing the upmost protection for long-term storage. Data on the micro-SD card would remain stored until the card was filled at which point the data logger was programmed to begin to overwrite the oldest of existing data. Thus, the ring memory cycle was generated helping to ensure data was stored locally for as long as possible enabling any break in remote communications to be restored and no data lost. Fortunately, communications were never lost long enough during Phase 2 testing to require this backup protocol.

The data loggers were constantly monitoring the sensors collecting measurements and processing the values against programming logic. However, data were only kept if a “trigger” was met. A trigger is a user-defined threshold defined within the data logger program that when encountered would prompt the data logger to record a data set to the micro-SD card. Generally, the data set would consist of many data every second over a set period, such as a few seconds leading up to the trigger and several seconds to a few minutes after. Recorded data prior to the trigger event is possible because the data logger, while constantly monitoring, is also temporarily storing the data into a buffer that can be permanently recorded upon trigger, and without a trigger is recorded over. The triggers used for monitoring, along with some of the programming logic, are described in the following sections.

CHAPTER 3. REVIEW OF FIELD DATA

FIELD TESTING

The field-testing program was comprised variable load long-term monitoring. Pluck tests were performed during Phase 1 field-testing to collect a benchmark set of data characterizing the dynamic response of each HMLT with a known load. These tests were not necessary during Phase 2.

Setup for the Variable Load Long-Term Monitoring

Instrumentation for the variable load long-term monitoring consisted of three primary sensors: strain gages, ice sensor, and anemometer. These sensors were installed, as described above, and as detailed in Appendix A of the Phase 1 report (Lloyd *et al*., 2020). Following sensor replacement, equipment maintenance, equipment box maintenance and other operational checks, the field team uploaded the long-term monitoring program to the datalogger and verified that communications with the modems were live and functioning properly. Then the equipment box was locked and sealed.

The long-term monitoring program collected several different types of data, as defined above. Ten-minute averages and maximums were recorded under the ambient data type. Once retrieved by the server at Purdue University, it was displayed for each test location on a website plotting wind direction and speeds on two wind roses, 10-minute wind maximums on a curve. An example of this website is shown in Figure 19 for the Baxter Interchange. The website also contained a tab displaying communication status and current battery bank voltage for each location as a quick check on these vital aspects of the DAQ system. In addition, wind tables were defined early in the monitoring program such that if a wind measurement was sampled above 40 mph or 50 mph, the data logger would begin a trigger event sequence. This entailed recording 200 data points prior to the trigger (or about 4 seconds of continuous), and 1000 data points following the trigger event (or about 20 seconds of continuous data). In addition to the wind speed triggers, peak stress triggers were also programmed such that if a stress measurement was sampled by the data logger above 5 ksi or below -5 ksi, or above 10 ksi or below -10 ksi, the data logger would initiate a trigger event sequence. In this case, similar to the wind speed triggers, the data logger would collect 200 data points leading up to the trigger and 1000, following. This means that the data logger was logging a data point from the anemometer, accelerometer, and the strain gages for the 24 seconds of triggered time-history data. Stress-based triggers were programmed for the case where low wind speeds might be able to excite large-amplitude vibrations in the pole.

In addition, the data logger was constantly monitoring output from the ice sensor. These data were sampled and stored independently of the wind and stress trigger events but following post processing of data the Research Team was able to correlate recorded icy conditions present with the different trigger events through a synchronized time stamp, thereby enabling the team to determine any potential relationship between the presence of ice and large-amplitude vibration.

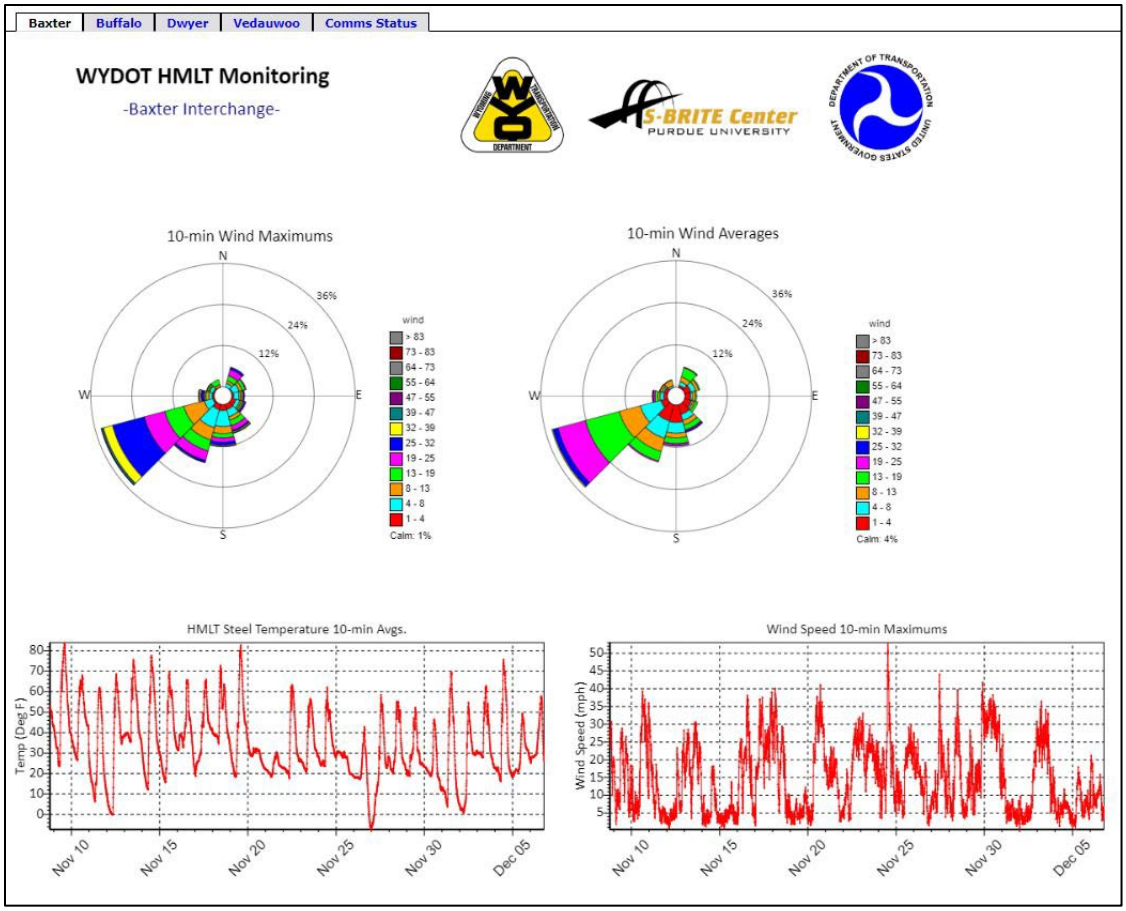

Figure 19. Web-based real time data display

Results of the Long-Term Monitoring

Based on previous field testing of HMLT's, it was known that large-amplitude mode I vibration occurrences were rare. A primary objective of the present research therefore was to record this type of structural response as many times as possible to better understand the correlating weather patterns and magnitude of the stress ranges it could cause. Previous research by Connor et al. (2012), as well as some amateur-captured video footage, showed evidence of large-amplitude vibration events, but little was known about the conditions that might cause it or the potential resulting damage.

Across-wind motion, indicating motion normal to the direction of wind, were most often observed by the Research Team. However, there were also indications of lesser frequent along-wind motion, or a movement parallel with the direction of wind due to buffeting of the pole, an example of which is pointed out in the discussion of field testing results. Across-wind vibration caused the largest stress ranges recorded throughout testing. There were two large-amplitude mode I lock-in events recorded during the 18 months of field monitoring. These are discussed in greater detail below.

Phase 2 monitoring of the poles began in September 2020 and concluded in March 2022. Within this period of time, many wind-based triggers occurred along with several stress-based triggers. The vast majority of these data presented typical behavior of the HMLTs, such as that shown in Figure 20. This figure is a double-y plot with stress plotted along the vertical left axis and wind speed along the vertical right axis. Both are plotted against the data time stamps on the horizontal axis. Two foil resistance strain gages from the Baxter Interchange HMLT are shown, representing the largest stress ranges measured in the pole during this event. FG(4) and FG(8) were located opposite each other centered on the flats that face approximately magnetic south-southeast and north-northwest, respectively. While the oscillation period and stress reversal are typical of most observed responses for all monitored HMLTs, the magnitude of the stress ranges shown here are among the larger stress ranges generally observed for typical wind-induced oscillations. Wind speed varied 10 mph between the low of 30 mph and high of 40 mph. The average wind speed over this period of time was 32 mph and the average direction was approximately 51 degrees, or heading southwest. No ice was reported at the time of the event. The frequency of vibration was approximately 4 cycles over 10 seconds, or 0.4 Hz, agreeing well with the mode I resonant frequency calculated for this HMLT using Phase 1 pluck test data. The strain gages measuring the largest stress ranges were therefore positioned along an axis perpendicular to the direction of wind, meaning that the oscillations were across-wind. This was the most common type of motion observed throughout testing, including the largest recorded event discussed later.

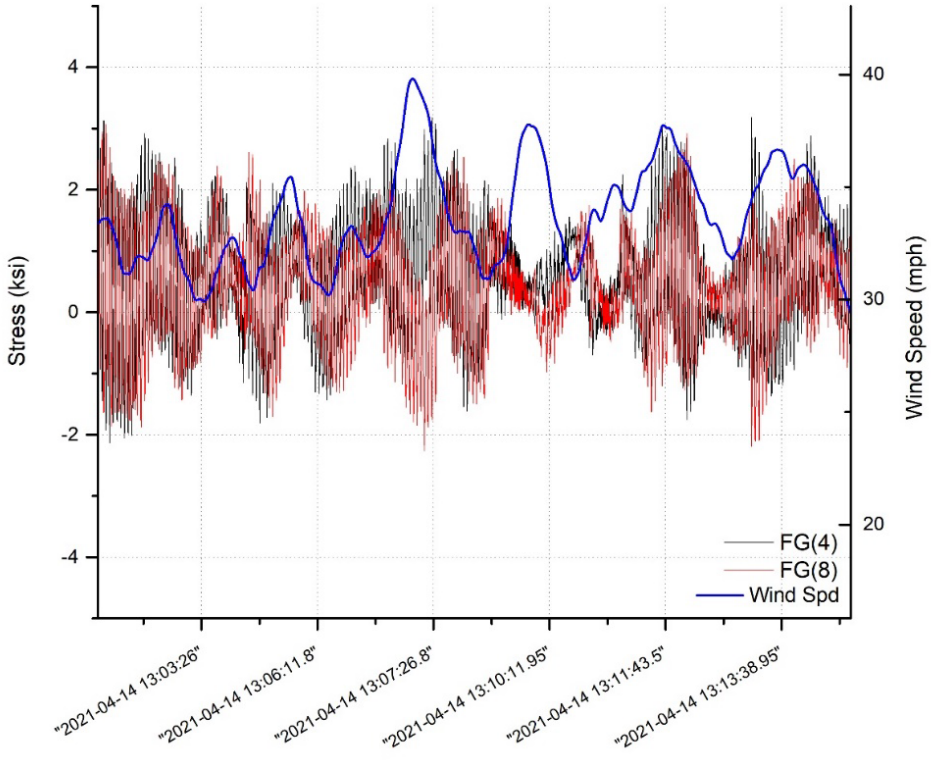

Figure 20. Data set from Baxter Interchange representing typical across-wind response

Another observation to make from Figure 20 is the seeming lack of correlation between wind speed and stress range. One might expect to observe that when the wind is blowing faster (i.e.

more energy to impart), the pole would respond with larger vibrations and therefore larger stresses measured in the tube wall. However, as can be seen in this figure, that is not always the case. The aeroelastic response of the towers is far more complex than this simple assumption. The primary driver for larger stress ranges is larger deflections. The deflections, specifically the across-wind deflections, are driven by a phenomenon called, vortex shedding. Vortex shedding is well known in wind engineering and is addressed directly in the AASHTO *Standard Specifications for Structural Supports for Highway Signs, Luminaires, and Traffic Signals*. Vortex shedding is the instance of alternating low-pressure zones downwind of a tower. The low-pressure zones generate lateral forces normal to the direction of wind driving the deflections. When the frequency of vortex shedding matches with the modal frequency of the tower, resonance occurs, amplifying vibrations with large forces and deflections. This is also referred to as lock-in condition. Vortex shedding is a complex structural response to air flow that is highly dependent upon the flow characteristics of the air itself and how those characteristics relate to the geometry and natural frequencies of the high mast tower. Interruptions in the vortex shedding through turbulent airflow and randomly fluctuating wind gusts makes correlating a pattern of structural behavior to wind speed nearly impossible. As was observed throughout Phase 1 monitoring, the large amplitude mode I vibration events are rare and unpredictable. This was again confirmed during Phase 2 field monitoring.

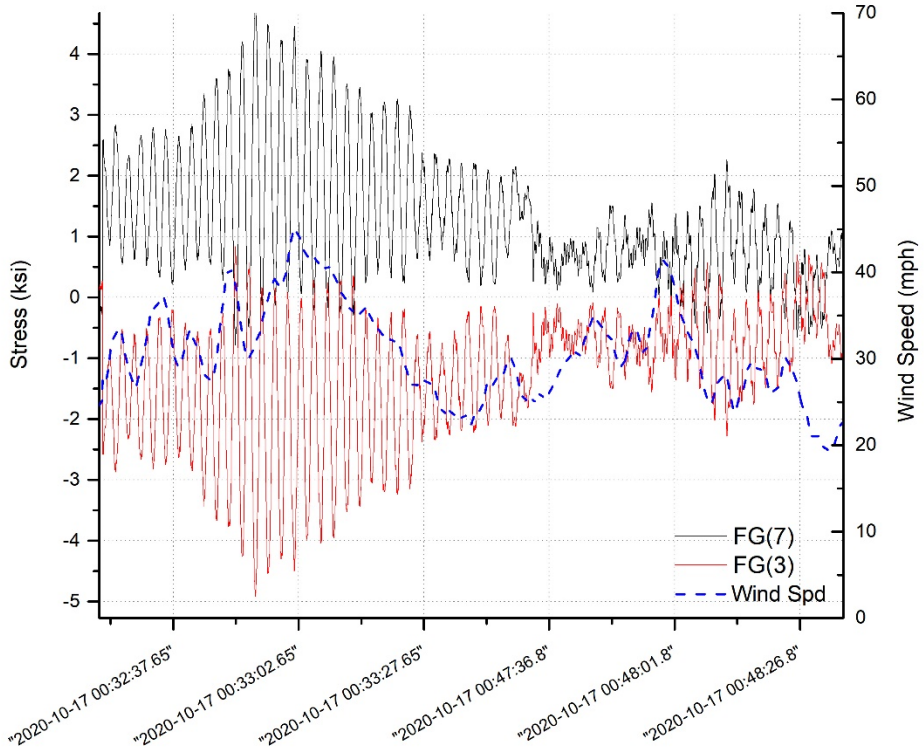

Figure 21. Data set from Buffalo Tri-Level representing typical along-wind response

Figure 21 displays a data set from the HMLT located at Buffalo Tri-level Interchange that was initiated by a Wind-40 trigger. This figure is a double-y plot with stress plotted along the vertical

left axis and wind speed along the vertical right axis. Both are plotted against the data time stamps on the horizontal axis. The data from two foil resistance strain gages are shown, representing the largest stress ranges measured in the pole during this event. FG(3) and FG(7) were located opposite each other centered on the flats that face approximately magnetic east and west, respectively. Wind speed varied 23 mph between the low of 22 mph and high of 45 mph. The average wind speed over this period was 26 mph and the average direction was approximately 302 degrees (i.e., south-southeast heading). No ice was reported at the time of the event. The frequency of vibration was again a mode I resonance matching measure frequencies from the original pluck test.

The strain gages measuring the largest stress ranges were therefore positioned along an axis nearly parallel to the direction of wind, meaning that the oscillations were mostly along-wind. However, in this particular case the wind heading was about 30 degrees off parallel alignment with these strain gages. This is not unexpected since in addition to the flexural response, the poles can also experience torsional effects caused by the wind. The stress ranges for this event were not much more than about 5 ksi. And as can be seen in the figure, FG(3) mostly measured tensile stress and FG(7) mostly measured compressive stress for this event, indicating that the pole was being bent in a similar direction as the wind heading such that it was a buffeting wind that pushed the HMLT nearly parallel to its path while simultaneously inducing smaller amplitude vibrations. Although along-wind response was not uncommon, it was rarer than across-wind vibrations. The deflection from the event plotted in Figure 21 would have been unremarkable to an observer in the area: taking the mean stress of each gage of about 1.75 ksi results in a calculated tip displacement of approximately 4.5 inches with vibrations resulting in ±3 – 8 inches.

Similar to Phase 1 monitoring, two stress-based triggers were programmed in addition to wind triggers, as discussed above; one for ±5 ksi and the other for ±10 ksi. This was done to ensure that large stress range events would be recorded if the wind speeds that caused them were less than 40 mph. Figure 22 shows a Stress-5 trigger event, meaning at least one of the strain gages measured a stress of greater than 5 ksi or less than -5 ksi. The event occurred at the Dwyer Junction HMLT. This figure is a double-y plot with stress plotted along the vertical left axis and wind speed along the vertical right axis. Both are plotted against the data time stamps on the horizontal axis. The data from two foil resistance strain gages are shown, representing the largest stress ranges measured in the pole during this event. FG(4) and FG(8) were located opposite each other centered on the flats that face magnetic south-southeast and north-northwest, respectively. Wind speed varied 27 mph between the low of 33 mph and high of 60 mph. The average wind speed over this period was 41 mph and the average direction was a consistent 260 degrees, or heading east.

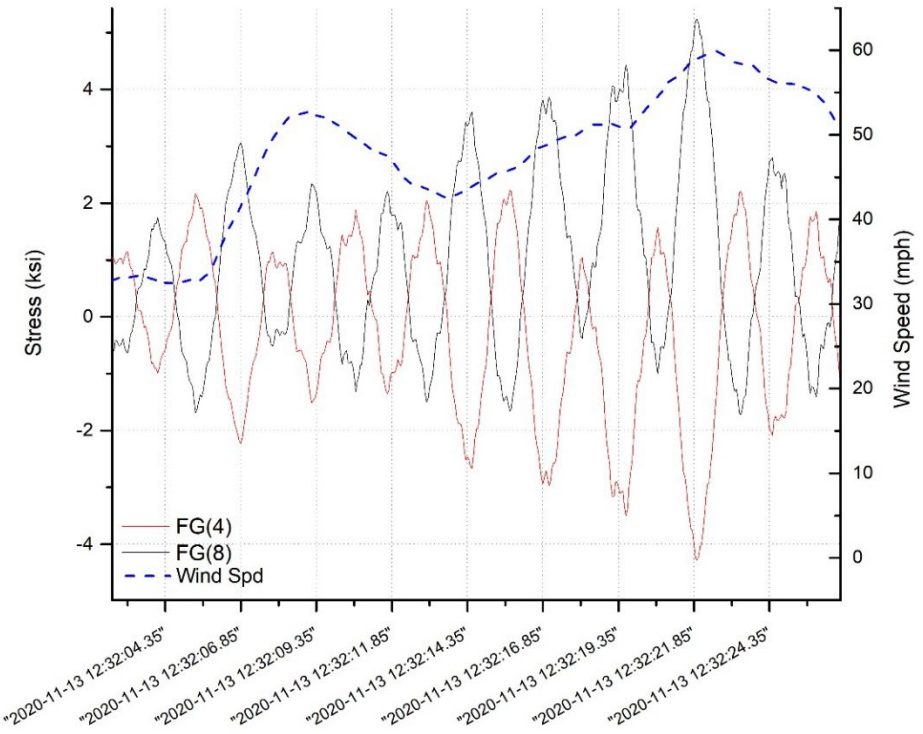

Figure 22. Data set from Dwyer Junction captured on a Stress-5 trigger

The peak stress range measured during this event was 9 ksi. There was no ice reported at that time. Direction of oscillation was nearly normal to the wind heading. The vibration frequency was close to 4 cycles over 10 seconds, or approximately 0.4 Hz. This frequency corresponded well with the calculated mode I resonant frequency for Dwyer Junction, found to be 0.40 Hz, as reported in the Phase 1 report (Lloyd *et al*., 2020). As can be seen on the figure, the oscillations resulted in complete stress reversal indicating typical mode I vibration. A calculation of tip displacement for the 9 ksi stress range is approximately ±12 inches (or a full range of motion of 24 inches). The event was recorded on a trigger that recorded 10 seconds of data prior to the trigger. This type of data buffer was used on all triggers in order to capture some data leading up to the trigger event to help show a more complete timeline of the structural response.

The event shown in Figure 23 was recorded at the Vedauwoo Interchange HMLT. The wind speed varied 23 mph between a low of 32 mph and high of 46 mph. The average wind speed over this period was 31 mph and the average direction was also 329 degrees, or heading south-southeast. The frequency of vibration was consistent with mode I resonant frequency of about 0.4 Hz and the motion was across-wind. There was no ice reported for the day of the event. The aerodynamic response was typical to most wind events for all of the monitored HMLTs throughout all of the field monitoring. All of the strain gages are plotted in this case to demonstrate the typical behavior with the largest stress ranges recorded in FG (2) and FG(6), normal to the direction of wind. The remainder of gages showed similarly symmetric measurements with declining magnitudes as the gages become more aligned with the direction of

wind heading. This indicates that the primary axis of flexural response was perpendicular to wind flow.

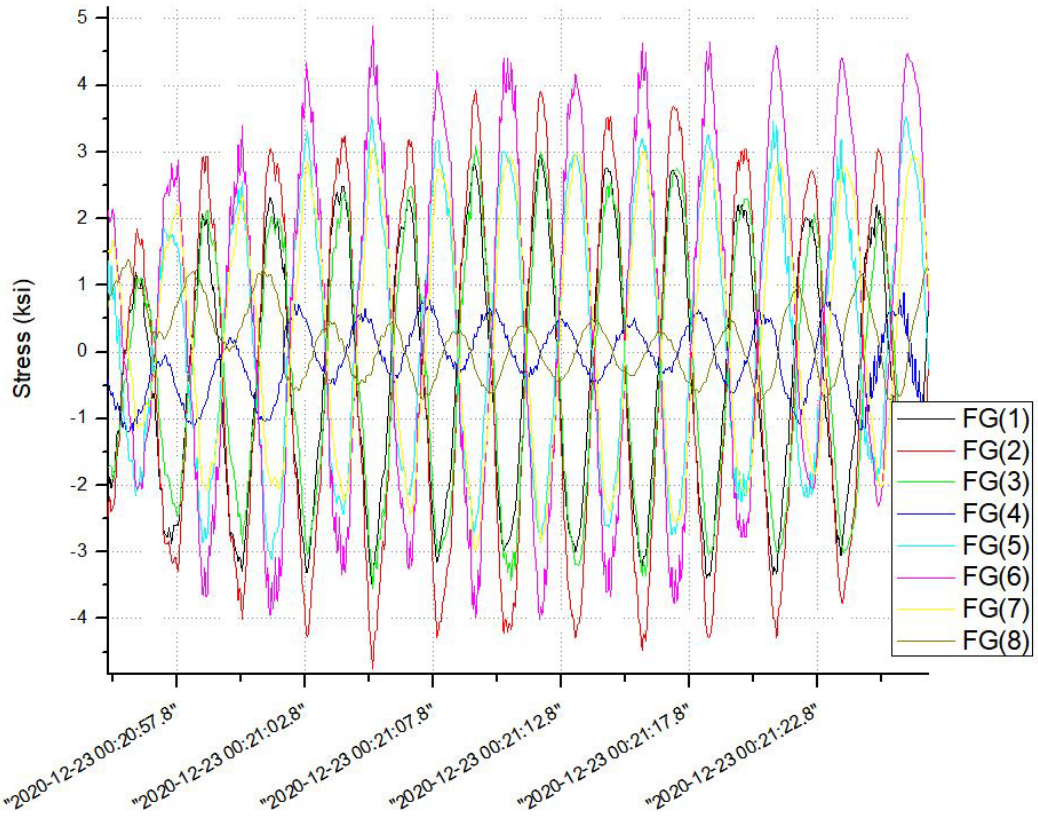

Figure 23. Data set from Vedauwoo Interchange captured on a Wind-40 trigger

Two additional medium-amplitude events were recorded at the Vedauwoo Interchange site during Phase 2 monitoring. The first event was initiated on a wind-40 trigger, and is plotted in Figure 24. This figure is a double-y plot with stress plotted along the vertical left axis and wind speed along the vertical right axis. Both are plotted against the data time stamps on the horizontal axis. The data from foil resistance strain gage are shown, representing the largest stress ranges measured in the pole during this event. FG(2) was located centered on the flat that faced approximately magnetic north-northeast. FG(6) is the strain gage positioned directly opposite of FG(2) and displayed symmetric measurements confirming the structural response. Wind speed varied 17 mph between the low of 28 mph and high of 45 mph. The average wind speed over this period was 34 mph and the average direction was about 324 degrees, or heading south-southeast. The vibration was across-wind motion with approximately 4 cycles over 10 seconds, or 0.4 Hz. This frequency matches the calculated mode I resonant frequency for Vedauwoo Interchange, reported for Phase 1 (Lloyd *et al*., 2020). A calculation of tip displacement for the approximately 8 ksi peak stress range is ±19 inches (or a full range of motion of 38 inches). Although there appears to be a gap in the data where the oscillation magnitudes drop from around 13 ksi to about 3.8 ksi, it was confirmed that there is none. A closer look at the data revealed that a gradual damping to about 8 ksi stress range was followed by a quick reduction to the smaller oscillations of about 3.8 ksi at a moment when the wind velocity momentarily dipped.

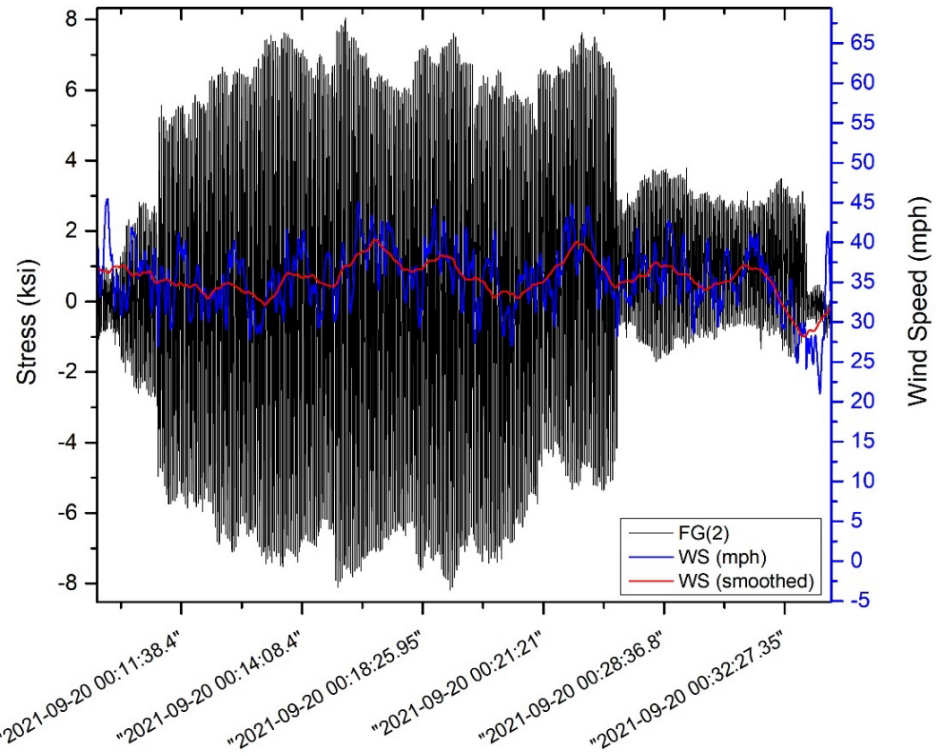

Figure 24. Medium oscillation data set from Vedauwoo captured on a Wind-40 trigger

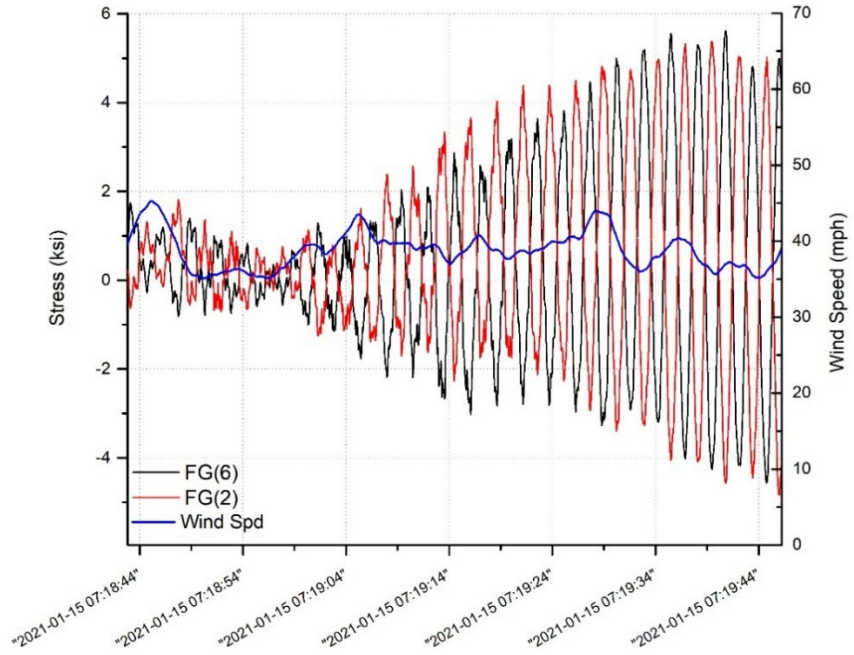

Figure 25. Data set from Vedauwoo Interchange captured on a Wind-40 trigger

The other medium-amplitude wind-40 trigger event for Vedauwoo Interchange is plotted in Figure 25, which occurred in January of 2021. There was no ice accumulation reported for the time of this event. This figure is a double-y plot with stress plotted along the vertical left axis and wind speed along the vertical right axis. Both are plotted against the data time stamps on the horizontal axis. The data from two foil resistance strain gages are shown, representing the largest stress ranges measured in the pole during this event. FG(2) and FG(6) were located opposite each other centered on the flats that face approximately magnetic north-northeast and south-southwest, respectively. Wind speed varied 10 mph between the low of 35 mph and high of 45 mph. The average wind speed over this period was 39 mph and the average direction was approximately 294 degrees, or primarily heading east-southeast. The displacement was across-wind motion at a frequency of 0.4 Hz. A calculation of tip displacement for the 5.6 ksi peak stress range is approximately ±14 inches (or a full range of motion of about 28 inches).

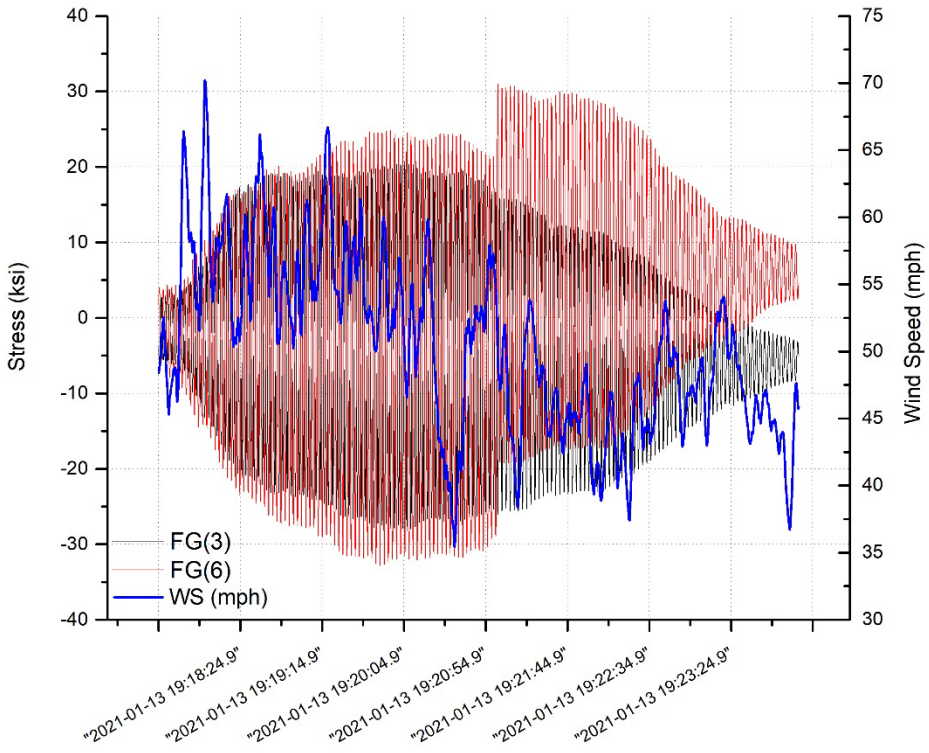

Figure 26. Large oscillation data set for Dwyer Junction captured a Wind-40 trigger

The two final triggered events to be discussed herein contained the largest amplitude oscillations observed throughout monitoring. Both events occurred at the Dwyer Junction location, which was also the location of the largest recorded event during Phase 1 monitoring, albeit a different pole. The first event was initiated on a wind-40 trigger and is plotted in Figure 26. This figure plots stress along the vertical left axis against the data time stamps on the horizontal axis. Data from two foil resistance strain gages, FG(3) and FG(6), are shown representing the largest stress ranges measured in the pole during this event. FG(3) was installed on the flat that faces approximately magnetic east and FG(6) was installed facing west-southwest. The wind speed has

also been included in Figure 26 where it can be seen that wind speed varied 35 mph between the low of 35 mph and high of 70 mph. The average wind speed over this period was 50 mph, and the average direction was approximately 320 degrees, or a heading of south-southeast. The vibration was across-wind motion at approximately 0.4 Hz, which matches the calculated mode I resonant frequency for Dwyer Junction, as reported in Phase 1 (Lloyd *et al*., 2020). A calculation of tip displacement for the -32.6 ksi minimum stress is approximately ±87 inches (or a full range of motion of 174 inches, which is equal to 14.5 ft.). The event ramps up around 7:18 pm on January 13, 2021, and lasts for about four minutes before beginning to dampen out, for a total event time of about 6.5 minutes.

Figure 27 zooms into the segment of largest stress range cycles from the lock-in event. It plots stress measurements from strain gages FG(3) and FG(6) on the right side vertical axis, against the time stamp along the horizontal axis. The left side vertical axis plots wind speed for the same period. Lock-in phenomena can be observed in the extreme magnitude of the stress ranges during which the pole was subjected to large-amplitude reversal displacements in mode I resonance.

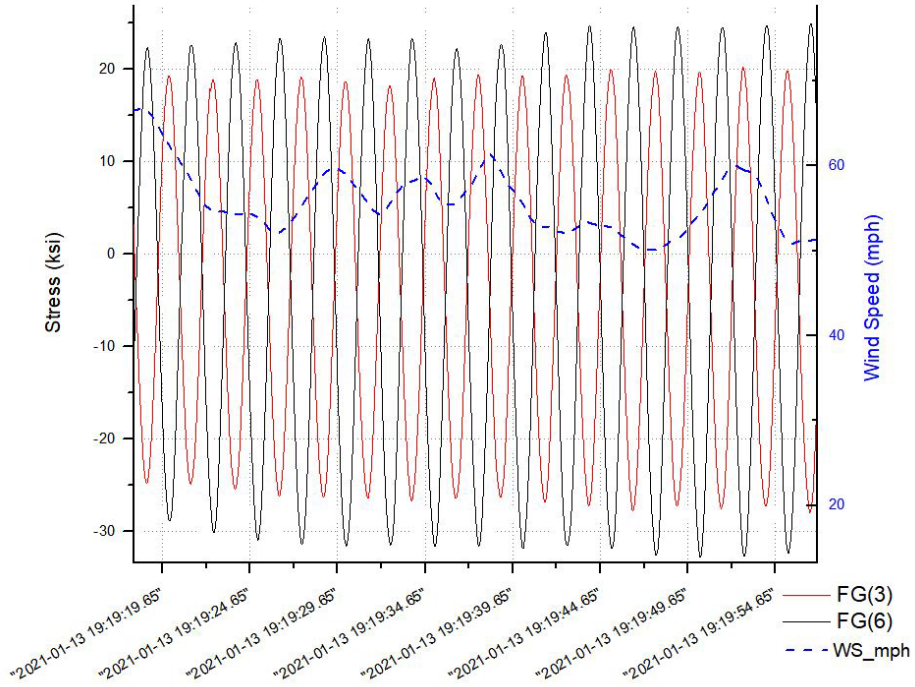

Figure 27. Thirty-five second data set showing lock-in phenomena at Dwyer Jct.

While Figure 26 indicates notable wind speed variability, smaller segments of time, such as shown in Figure 27, reveal that the wind speed remained relatively constant over sufficient periods to energize the structural oscillation. Within a few hours of the recorded event shown in Figure 26, a WYDOT employee visited the pole location and took a photograph of the pole with ice accumulation on one side. This is shown in Figure 28. Temperature of the steel was shown to have dropped 20° F over the course of 25 minutes to about 30° F, making the ice build-up possible. Since the peak stress range measurements observed during the event were consistently seen for FG(3) and FG(6), it can be said that the direction of displacement did not vary

significantly. It also indicates that the pole was oscillating along the approximate axis between these two strain gages, as labeled in Figure 29 with the golden arrow. The arrow is meant only to approximate the direction of motion of the pole. Wind direction has also been labeled on the figure using a black arrow, which was taken from wind direction data recorded from the anemometer during the event. Wind direction varied up and down a few degrees, remaining relatively consistent out of the west-northwest direction and heading east-southeast (or approximately 320 degrees). The wind direction corresponded with the peak stress measurements in FG(3) and FG(6) for cross-wind vibration. A minor difference for this event can be seen Figure 30 where buffeting of the pole is also indicated in strain gages FG(4) and FG(8). This behavior is most obvious at the beginning of the data set when the sudden burst of 70 mph wind gusts impacted the pole. FG(8) measured small cycles in tension at the same time that FG(4) measured small cycles in compression without making full reversals (i.e., mean stress was not near zero). FG(4) and FG(8) measured stress ranges of about 18 ksi, each with a mean stress that was opposite each other in sign. Hence, the data suggests that the pole was pushed in flexure, aligned with the direction of wind, while it began to oscillate orthogonally to the wind vector, resulting in a combination of buffeting and vortex shedding. This is most likely why the peak stress ranges are being measured by two gages that are not directly across from each other.

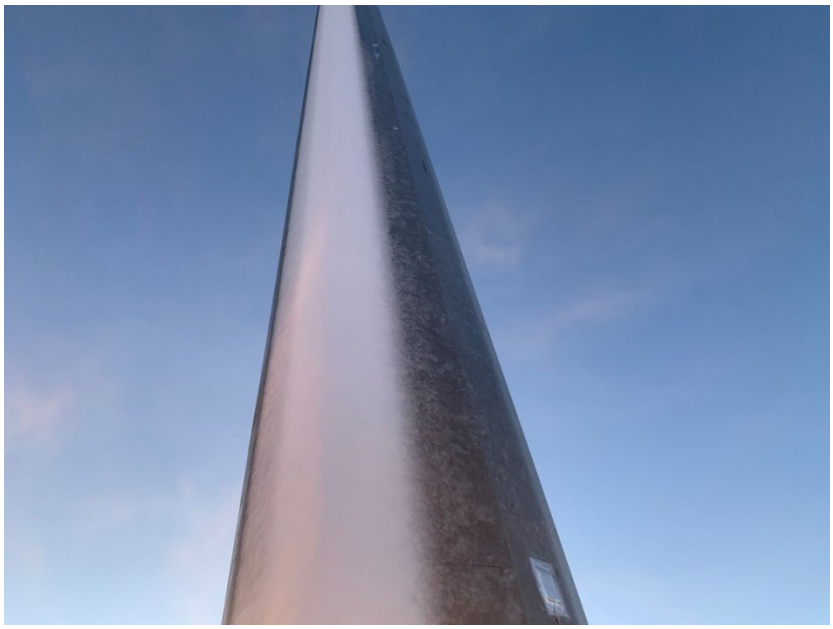

Figure 28. Photograph of accumulated ice witnessed by WYDOT employee

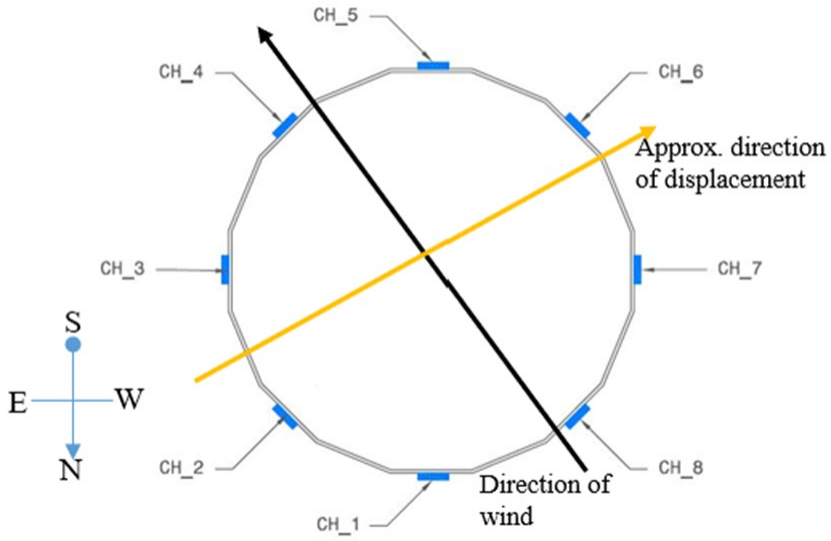

Figure 29. Planview diagram of the large amplitude event at Dwyer Jct HMLT Jan 13, 2021

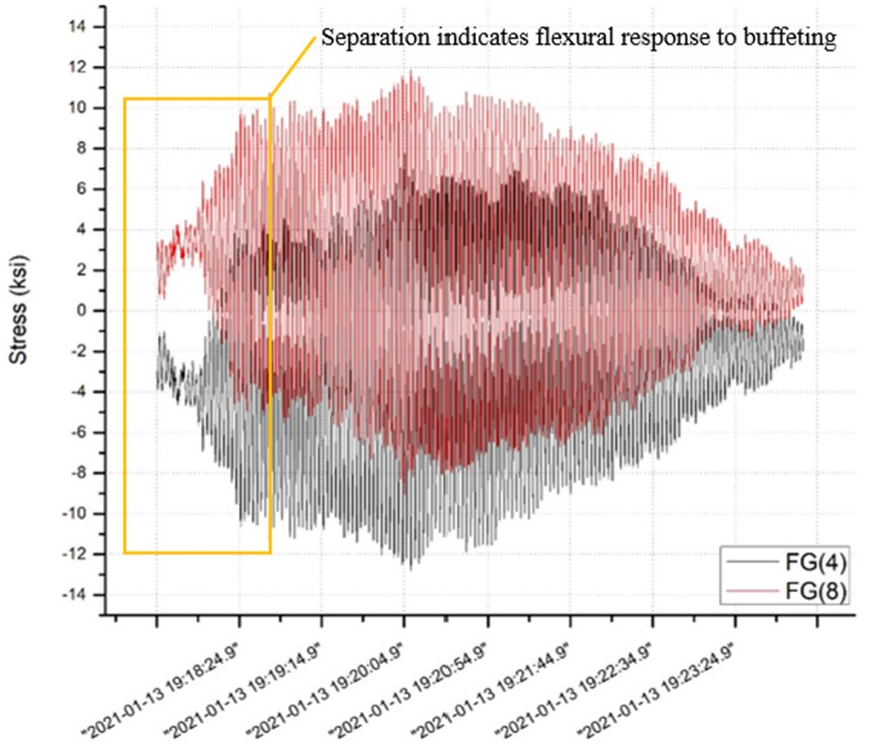

Figure 30. Large oscillation data set for Dwyer Junction showing indications of buffeting

The second of the two large-amplitude events observed during Phase 2 monitoring also occurred at the Dwyer Junction location. On March 29, 2022, a winter storm blew through the area-exciting mode I large-amplitude resonance in several HMLTs in the vicinity of Dwyer Junction.

Data was only being collected on one pole; however, a WYDOT employee was also in the area and captured cell phone video footage of other poles experiencing large amplitude vibration from the same storm. Figure 31contains two still images taken from the amateur video at the approximate moment of largest deflections of the two poles. A crude estimate of the top deflection appears consistent with calculations based on maximum stress measurements recorded on the monitored pole (i.e., ±74 inches). Additionally, the pole on the left side of the figure shows an accumulation of snow. Ice accumulation was not reported by the monitoring system.

Figure 31. Images from cell phone footage showing deflection of two poles

The pole was oscillating along the approximate axis between gages FG(2) and FG(6), as labeled in Figure 32 with the golden arrow. The arrow is meant only to approximate the direction of motion of the pole. Wind direction has also been labeled on the figure using a black arrow, which was taken from wind direction data recorded from the anemometer during the event. Figure 33 plots the entire data set captured for the March 29, 2022, event, which was initiated on a wind-40 trigger. This figure plots stress along the vertical left axis against the data time stamps on the horizontal axis. Data from one foil resistance strain gage, FG(6), are shown representing the largest stress ranges measured in the pole during this event. FG(6) was installed facing west-southwest. The wind speed has also been included in Figure 33 where it can be seen that wind speed varied 22 mph between the low of 29 mph and high of 51 mph. The average wind speed over this period was 37 mph, and the average direction was approximately 338 degrees, or a heading of south-southeast. Wind direction varied up and down a few degrees, remaining relatively consistent. The wind direction corresponded with the peak stress measurements in FG(2) and FG(6) for crosswind vibration. The vibration was across-wind motion at approximately 0.4 Hz, which matches the calculated mode I resonant frequency for Dwyer Junction, as reported in Phase 1. A calculation of tip displacement for the 28 ksi maximum stress is approximately ±74 inches (or a full range of motion of 148 inches, which is equal to approximately 12 ft.).

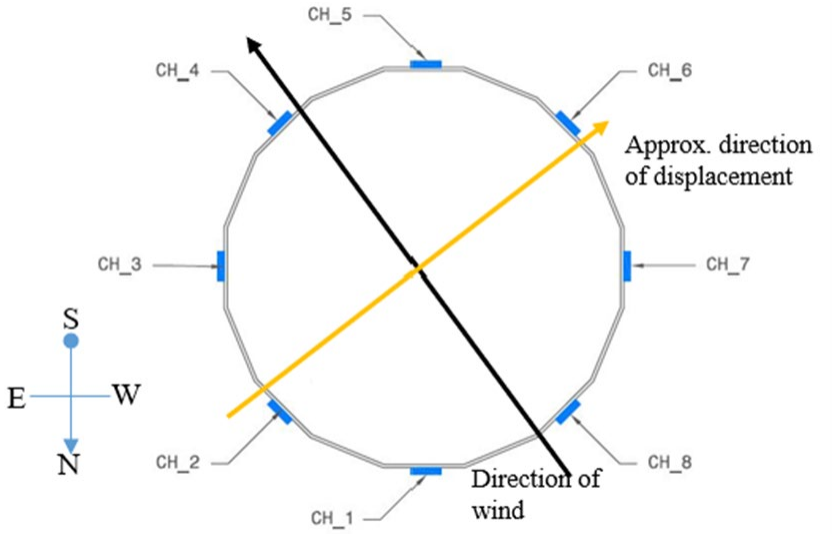

Figure 32. Planview diagram of the large amplitude event at Dwyer Jct HMLT Jan 13, 2021

Figure 33 is nearly a continuous data set, with some minimal time gaps between trigger events. Several small chronological gaps in the data do exist. This is due to the parameters of the trigger programmed into the data logger combined with the frequency of 40 mph gust occurrences. As the event continued, the data logger would complete the required number of records for a single event before a logic test on buffered data sampling could trigger recording again. Thus, if the time that elapsed between the completion of a trigger record and a new trigger (i.e., another wind speed measurement greater than or equal to 40 mph) exceeded 10 seconds, a gap in the timeline would occur. This does not result in a significant loss of information but understanding this helps explain any abrupt changes in oscillations, such as can be seen at the end of the data set shown in Figure 34. Due to the density of the data at the scale plotted in Figure 34, a smaller subset of data are plotted in Figure 35. In this figure it can be seen that the maximum stress range measured for FG(6) was about 53 ksi (maximum stress of 28.7 ksi and minimum stress of -24.3 ksi). Additionally, at this plot scale it can be observed that the wind was relatively constant at about 40 mph, which is consistent with the measured average of 37 mph.

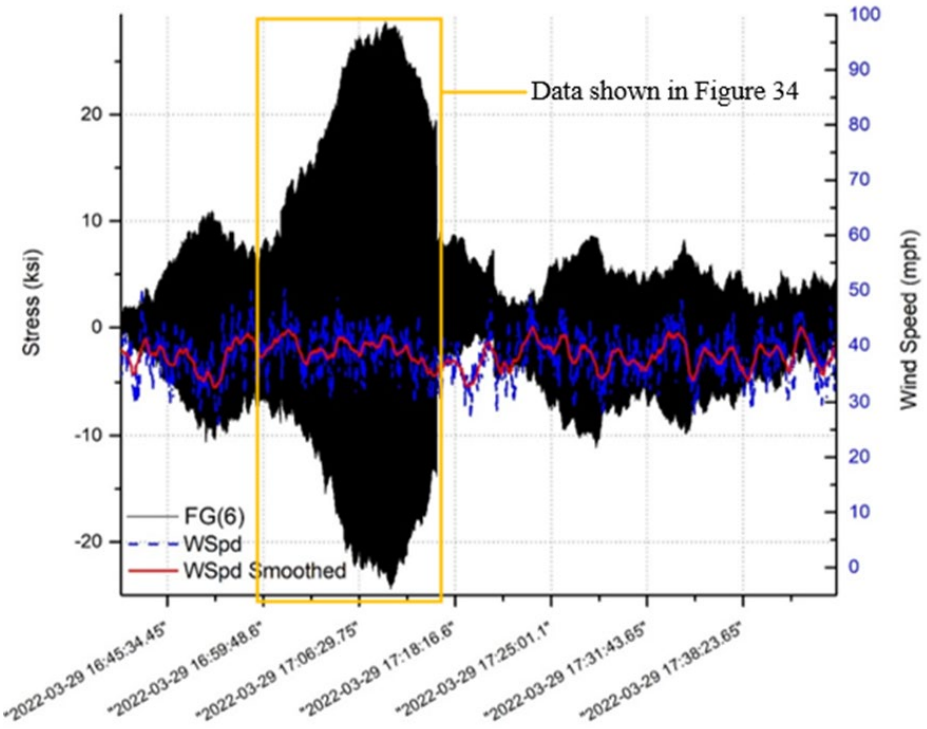

Figure 33. Stress-time data set for Dwyer Junction from March 29, 2022, storm

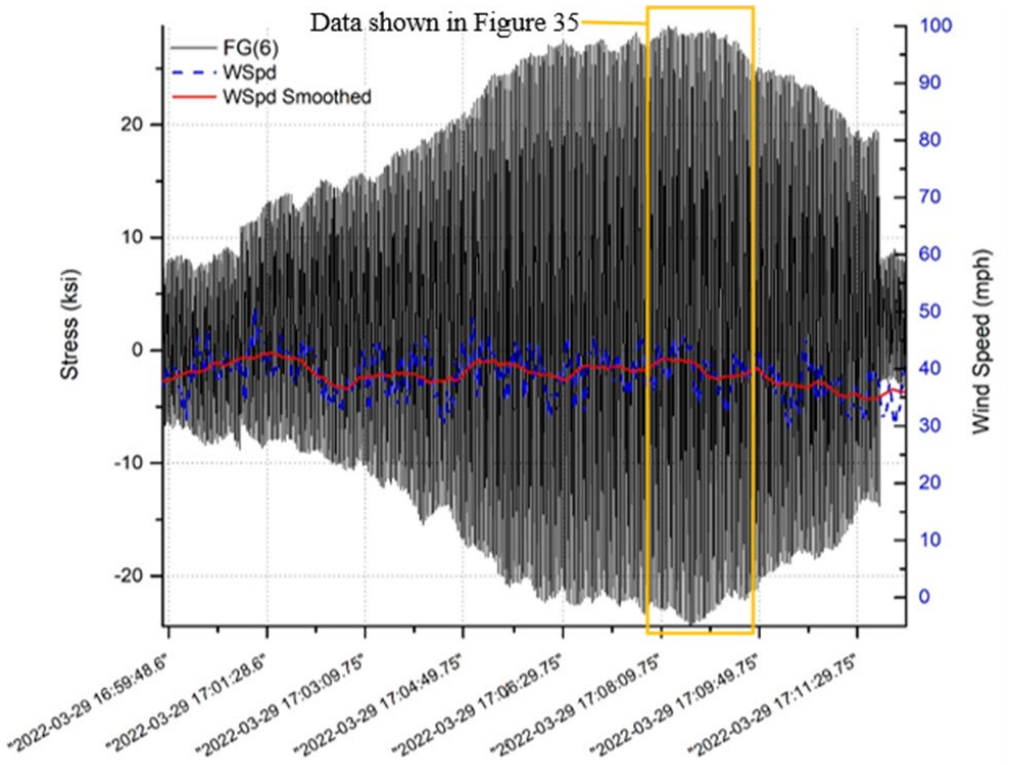

Figure 34. Large oscillation data set for Dwyer Junction captured a Wind-40 trigger

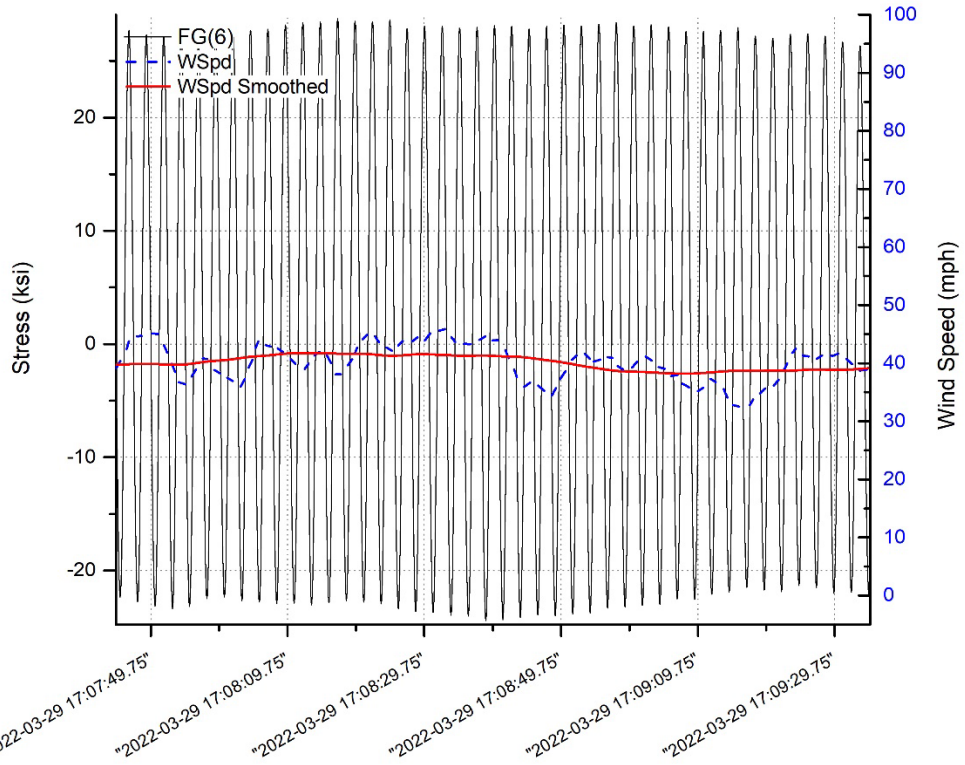

Figure 35. Zoom-in of large amplitude data for March 29 Dwyer Junction event

Results of the Fatigue Life Evaluation

Data gathered during the long-term monitoring were used to perform a fatigue life analysis for each HMLT. The fatigue evaluation was performed using the AASHTO nominal stress approach for the tube wall-to-base plate weld detail using the measured stress, taken at seven feet above the base plate. Then an extrapolation factor was calculated for the nominal stress at the base plate weld. This was performed using mechanics equations found in *Deflections and Stresses in Circular Tapered Beams and Poles* by William McCutcheon (1983). The extrapolation factor used to convert the measured stress at seven feet above the base plate to the nominal stress at the base of the HMLT was 1.06 (or a 6 percent increase). The extrapolation factor was applied to the average bin stress range amplifying the effective stress range calculation for the base plate weld detail.

Rainflow cycle counting was used to create stress range histograms for the eight strain gages included in the monitoring of the weld detail. Applying a mathematical cumulative damage model called Palmgren Miner's Rule to the stress-range histograms, the effective stress range was calculated for the base plate weld detail associated with each strain gage locale. The effective stress range is commonly used as a constant stress range value to compute the expected fatigue life for a variable stress range record. Equation (1) is the equation used to calculate the effective stress range; where S_{reff} is the effective stress range, $f_i = N_i/N$, N_i is the number of cycles for the specific stress range bin, N is the accumulated total number of cycles for all stress range

bins, and S_{ri} is the stress range for the specific stress range bin. Knowing the effective constant amplitude stress range, the fatigue life was calculated for each of the long-term monitoring strain gage locations. This is the same calculation performed during Phase 1 reporting (Lloyd *et al*., 2020).

Equation (1) $$S_{reff} = \sum\left(f_i * S_{ri}^{3}\right)^{1/3}$$

Prior to presenting the results from the fatigue evaluation, it is important to discuss how the data were analyzed. The data logger used for the study was capable of creating histograms based on the Rainflow cycle counting method. The stress-range histograms were created with all bins equally sized at 0.5 ksi. This was true except for the first bin, which excluded all cycles less than 0.25 ksi (i.e., the first bin ranged from 0.25 ksi to 0.5 ksi). The data logger was programmed to perform the Rainflow cycle count algorithm once every ten minutes and place all load cycles in their respective bins for each channel, for that period. For example, if channel 1 measured a single load cycle ranging 1.4 ksi in a given 10 minute interval, the data logger would record 1 cycle in the 1.5 ksi bin. This would be done because the 1.5 ksi bin includes all cycles between 1 ksi and 1.5 ksi, with an average of 1.25 ksi. This process is iterated every ten minutes building the histograms used to evaluate remaining fatigue life, the results of which are summarized in Table 2. The individual stress range histograms for each HMLT are provided in Appendix A of this report.

Once the final histograms were compiled for each strain gage (i.e., at the completion of the monitoring), a truncation was performed based on the AASHTO fatigue category appropriate for the structure detail being monitored. The truncation disregarded all cycles below a given bin. Disregarding the lower bins of a histogram is a common practice in a fatigue analysis. This is typically done so the effective stress range is not artificially reduced by the high number of very small stress range cycles, often attributed to signal "noise". A cutoff value that corresponds to between 1/4 and 1/3 of the constant amplitude fatigue limit (CAFL) of a detail is commonly used. In the case of the present research, a Category E' detail with a CAFL of 2.6 ksi was truncated such that all cycles less than 0.75 ksi were omitted. Following truncation, the effective stress range for each strain gage was then calculated using Palmgren Miner's Rule. It is noted that when calculating the effective stress range the average stress range for the bin was used. The fatigue life, as seen in Equation (5), is a function of the effective stress range. Truncating raised the effective stress range estimate, which in turn slightly reduced estimated fatigue life.

Fatigue life estimates were made for each of the strain gage locations in this study using the effective stress range and truncated histograms. Based on detail category and the truncated histogram of each strain gage, the percent of cycles exceeding the CAFL was also computed. If the number of cycles exceeding the CAFL was less than 1:10,000 (0.01 percent), the detail was determined to have infinite fatigue life. However, if more than 1:10,000 cycles exceeded the CAFL, the detail was determined to have finite fatigue life. Finite fatigue life, N_f, was computed by dividing the detail constant, A, for a given fatigue category by the detail's cubed effective stress range, S_{reff}, as shown in Equation (2).

Equation (2) $$N_f = \frac{A}{S_{reff}^{\ 3}}$$

Next, the difference between the total fatigue life, N_f, and the amount of fatigue life used to date (structure's age), N_{used}, was computed revealing the amount of remaining fatigue life, N_r, as shown in Equation (3). The HMLT date on the construction plans for each site was used to calculate the remaining fatigue life at the time of the report.

Equation (3) $$N_r = N_f - N_{used}$$

One final important note is that fatigue life estimates (of existing structures) can range anywhere from negative years (i.e., the amount of used fatigue life is greater than the available fatigue life) up to thousands of years. Since no one can accurately predict what will happen to a structure in 100 years, let alone over 1000 years, one of three conclusions is expressed for the remaining fatigue life of a given detail: numerical between 0 and 100 years, > 100 years, or infinite. Infinite life applies to locations where the detail CAFL was not exceeded more than 0.01 percent (1/10,000). A brief summary of the fatigue life analysis results for Phase 2 are provided in Table 2. The strain gage representing the shortest fatigue life for each pole is listed in the table. The complete stress range histograms and fatigue life calculations for Phase 2 monitoring are provided in detail in Appendix A of this report. Table 3 summarizes the fatigue analysis of all Rainflow data combined from Lloyd *et al*. (2020) and Phase 2 monitoring, comprising about 3 ½ years of data. Due to the larger data set represented by Table 3, it can be assumed that it best represents the remaining life of the welded base plate detail of the monitored HMLTs. Comparing data from Lloyd *et al*. (2020) to Phase 2 data it can be seen that the effective stress ranges were very similar or identical for each phase. The difference in fatigue life between the two phases of monitoring was the number of stress cycles in Phase 2, as compared to Lloyd *et al*. (2020), which in some cases was doubled or more. Appendix B of this report provides the complete stress range histograms and fatigue life calculations for the combined data from both phases of monitoring.

Table 2. Summary of Fatigue Life Evaluations for Phase 2 monitoring

Truncation		0.375 ksi		0.75 ksi			
Location	Gage ID	S_{reff}	% Exceedance	S_{reff}	% Exceedance	Cycles/ Day	Remaining Life (Yrs)
Baxter Int.	FG(3)	1.2	1.10	1.7	4.43	4,048	46.8
Buffalo Tri-Level	FG(4)	1.1	0.89	1.6	4.14	1,285	> 100
Dwyer Jct.	FG(1)	1.3	3.36	1.8	10.5	9,732	10.8
Vedauwoo Int.	FG(6)	1.3	4.07	1.8	13.16	18,856	-8.9

Table 3. Summary of Fatigue Life Evaluations for Combined Phase 1 and 2 monitoring

Truncation		0.375 ksi		0.75 ksi			
Location	Gage ID	S_{reff}	% Exceedance	S_{reff}	% Exceedance	Cycles/ Day	Remaining Life
Baxter Int.	FG(3)	1.1	1.04	1.7	4.45	2,369	86.7
Buffalo Tri-Level	FG(2)	1.0	0.21	1.5	1.60	1,111	> 100
Dwyer Jct.	FG(1)	1.2	2.52	1.8	5.07	4,326	36.9
Vedauwoo Int.	FG(5)	1.3	3.07	1.8	10.74	14,785	-5.5

CHAPTER 4. FINDINGS, CONCLUSIONS & RECOMMENDATIONS

FINDINGS

The following conclusions are the result of a nearly four-year study that included field monitoring in two phases of five high mast lighting towers at four locations within Wyoming. The primary objective was to observe a rare lock-in event generating high amplitude displacements and stress ranges in one or more of the HMLTs, which prior to this study, had been observed only in amateur video by passers-by. Some limited data was also observed by Connor et al. (2012), but without conclusive evidence. Two large-amplitude events were observed during Phase 1 monitoring (two-year study) reported previously and two additional large amplitude events were recorded during Phase 2 (18-month study) reported herein. In addition to the large amplitude events, there were several other notable events with relatively significant stress ranges recorded.

Similar to Phase 1 monitoring, the large-amplitude events recorded during Phase 2 took place at Dwyer Junction. The first was in January 2021, resulting in peak stress range of about 57 ksi (174-inch calculated tip displacement range) and total duration of about 3 minutes. The second event was recorded in March 2022, resulting in a peak stress range of about 53 ksi (148-inch calculated tip displacement range) and total duration of about 18 minutes.

Prior to the Phase 1 study, it was not understood what the magnitude of stress ranges might be induced in an HMLT during a large-amplitude mode I lock-in event. This has now been observed in both Phases of field study. Table 4 summarizes the general observations for each of the four largest-amplitude events recorded during both phases of field monitoring to compare side-by-side. The wind speeds are relatively similar for each event and ice or snow were reported for all cases. Other relatively large events were also observed during both phases of study for which no ice or snow were reported. However, in each of those cases the stress range maximums were less than half of those reported in Table 4. It cannot be concluded whether or not this observation is coincidental. A final observation is that the prevailing wind direction during all large events appears to correlate with the position of a corner of the tube wall. It is difficult to confirm this due to the variable nature of wind, but could help understand why resonance (i.e., lock-in) occurs in some cases and not in others when all other parameters are similar.

Table 4. Summary of Large Amplitude Oscillation Events for All Phases of Monitoring

Location	Date	Avg Wind Speed (mph)	High Wind Speed (mph)	Low Wind Speed (mph)	Ice Reported	Comment
Dwyer	Apr 2018	28-37	52	26	Yes	Ice reported minutes before event
Dwyer	Oct 2019	37	58	31	Yes	Ice reported 2 hrs prior to event
Dwyer	Jan 2021	50	70	35	No	Snow on the HMLT observed by WYDOT
Dwyer	Mar 2022	37	51	29	No	Snow on the HMLT observed by WYDOT

CONCLUSIONS

Observed behavior (both via collected data and amateur video capture during the time of field monitoring) in the high mast lighting towers was consistent with that associated with vortex shedding. Vortex shedding has been studied for several decades. It was addressed directly in the AASHTO *Standard Specifications for Structural Supports for Highway Signs, Luminaires, and Traffic Signals*. Vortex shedding is the instance of alternating low-pressure zones downwind of a tower. The low-pressure zones generate lateral forces normal to the direction of wind causing across-wind deflections. When the frequency of vortex shedding aligns with the modal frequency of the tower, resonance occurs, amplifying vibrations that result in large deflections. This is also referred to as lock-in condition. Vortex shedding is a complex structural response to air flow that is dependent upon the air flow characteristics itself and how those characteristics relate to the geometry and natural frequencies of the high mast lighting tower. Variable wind speeds that occur during typical storms tend to disrupt the vortex shedding frequency through turbulent flow, which can lead to an interruption of resonance that leads to damping, and the eventual end to large-amplitude oscillations. Evaluating for vortex shedding using equations from the AASHTO Standard Specifications suggests that tapered, multi-sided lighting towers have relatively low critical wind velocities for vortex shedding to occur (e.g. 2-6 mph). This is consistent with findings from Magenes (2011) who found that at wind speeds of 7 mph HMLTs were excited into mode II vortex shedding. However, the low wind velocities do not impart sufficient energy to excite the structures to large-amplitude vibration. Therefore, it could be argued that these are not the critical speeds. The range of 10-min wind speed averages for the four large-amplitude events captured during both phases of monitoring was between 28 and 50 mph. The average of the 10-min average wind speeds was 39 mph, suggesting that the critical wind speed for vortex shedding for these particular poles is more like 39 mph.. Commentary under article 11.7.2 in the AASHTO *Standard Specifications* states that observations and studies indicate that tapered poles can experience vortex shedding in second or third mode vibrations, and that those vibrations can lead to fatigue problems. Phase 1 of this study demonstrated, and Phase 2 has confirmed, that tapered poles are also susceptible to mode I vibrations resulting from vortex shedding, capable of imparting large-amplitude deflections that can cause significant fatigue damage. Equivalent static pressure design approaches may not be sufficient, nor economical, to remedy this complex phenomenon and it is the opinion of the Research Team that the best approach to mitigation is

through a mechanical mitigation strategy such as tuned mass damping or strakes. See Connor et al. (2012) for more information on the use and benefit of strakes for HMLTs.

The present study further resulted in the following conclusions:

- Large-amplitude mode I vibration is a rare occurrence. During Phase 2 monitoring there were two such events while monitoring four HMLTs continuously for 18 months. The first produced a maximum stress range of about 57 ksi. The second produced a maximum stress range of about 53 ksi. A third event produced stress range of 16 ksi, which is also considered a notable event.
- The typical effective stress range resulting from daily vibrations under normal wind conditions was once again found to be 1.7 ksi, consistent with Phase 1 monitoring.
- The HMLTs were found to be in the finite fatigue life regime with varying amounts of fatigue life remaining, ranging from negative to over 100 years. Fatigue life estimates were reduced during Phase 2 testing, primarily due to more stress cycles than counted during Phase 1 testing.

RECOMMENDATIONS

The following two recommendations resulted from the present study:

- Explore options to mechanically mitigate the resonant response that results in large-amplitude structural oscillation in the HMLT to protect against the rapid fatigue damage accumulation resulting from a lock-in phenomenon. This strategy can help prolong the fatigue life of existing HMLTs.
- Future research, including experimental fatigue testing of several HMLTs subjected to stress ranges similar to that observed during the several large-amplitude events at Dwyer Junction. The large-amplitude stress ranges observed in the laboratory setting would allow researchers to determine what local behavior is occurring and what factors are contributing to fatigue damage. Following large-amplitude cycling, continue testing the HMLTs applying more typical high-cycle fatigue stress ranges to determine what the fatigue life might be following such large-amplitude cycles when accounting for localized effects.

REFERENCES

Connor, R. J., Collicott, S. H., DeSchepper, A. M., Sherman, R. J., & Ocampo, J. A. (2012). *Development of Fatigue Loading and Design Methodology for High-Mast Light Poles*. NCHRP Report 718. Washington, DC: Transportation Research Board.

Lloyd, J. B., Connor, R. J., and Sherman, R. J. (2020). *Field Testing and Long-term Monitoring of Selected High-Mast Lighting Towers*. Report WY-20/04F. Wyoming Department of Transportation.

Magenes, L. (2011). *Fatigue Assessment of High Mast Illumination Poles Using Field Measurements*. Master's Thesis, University of Texas at Austin.

McCutcheon, W. J. (1983). *Deflections and Stresses in Circular Tapered Beams and Poles*. Civil Engineering for Practicing and Design Engineers. 2: 207-233. US Department of Agriculture, Madison, WI.

Nasouri, R., Nguyen, K., Montoya, A., Matamoros, A., Bennett, C., and Li, J. (2019a). *Simulating the Hot Dip Galvanizing Process of High Mast Illumination Poles. Part I: Finite Element Model Development*. Journal of Construction Steel Research, Volume 162.

Nasouri, R., Nguyen, K., Montoya, A., Matamoros, A., Bennett, C., and Li, J. (2019b). *Simulating the Hot Dip Galvanizing Process of High Mast Illumination Poles. Part II: Effects of Geometric Properties and Galvanizing Practices*. Journal of Construction Steel Research, Volume 159.

Sherman, R. J., and Connor, R. J. (2019). *Development of a Fatigue Design Load for High-Mast Lighting Towers*. Journal of Structural Engineering, Volume 145, Issue 1

APPENDIX A – PHASE 2 STRESS RANGE HISTOGRAM DATA

Table 5. Baxter Interchange Phase 2 Stress Range Histogram Data

RANGE	R AVG	CH 1	CH 2	CH 3	CH 4	CH 5	CH 6	CH 7	CH 8
0.25	0	0	0	0	0	0	0	0	0
0.5	0.375	0	16552103	16593131	25701956	28327951	21912950	8474570	25160364
1	0.75	0	5878594	6322920	9214194	10177343	7012080	3105584	8802900
1.5	1.25	0	1009206	1331632	1559186	1599203	1188164	678658	1485769
2	1.75	0	438683	502780	453826	407601	402586	376281	447260
2.5	2.25	0	115817	165561	110928	112551	98447	100619	109499
`3	2.75	0	29939	59007	28982	37060	26135	27568	28362
3.5	3.25	0	8760	22615	9093	12195	5392	8522	8428
4	3.75	0	2320	8461	3249	4404	1177	3109	2937
4.5	4.25	0	608	2182	1319	1926	312	2159	1167
5	4.75	0	179	560	512	976	86	640	535
5.5	5.25	0	45	32	183	507	19	317	196
6	5.75	0	14	7	53	356	3	179	112
6.5	6.25	0	8	0	32	235	6	127	81
7	6.75	0	2	1	18	187	0	130	50
7.5	7.25	0	0	0	14	175	1	114	37
8	7.75	0	1	0	10	145	1	49	48
8.5	8.25	0	1	0	1	131	0	30	71
9	8.75	0	0	0	4	115	0	38	75
9.5	9.25	0	0	0	1	122	0	41	124
10	9.75	0	0	0	2	97	0	31	177
10.5	10.25	0	0	0	0	94	0	17	143
11	10.75	0	0	0	1	82	0	19	61
11.5	11.25	0	0	0	0	60	0	11	40
12	11.75	0	0	0	0	76	0	12	33
12.5	12.25	0	0	0	0	56	0	10	49
13	12.75	0	0	0	0	74	0	9	68
13.5	13.25	0	0	0	0	64	0	7	69
14	13.75	0	0	0	0	46	0	10	82
14.5	14.25	0	0	1	0	63	1	5	38
15	14.75	0	0	1	1	32	0	8	32
15.5	15.25	0	0	3	0	0	0	3	32
16	15.75	0	0	0	0	0	0	4	33
16.5	16.25	0	0	0	0	0	0	7	0
17	16.75	0	0	0	0	0	0	1	2
17.5	17.25	0	0	0	0	0	0	4	0
18	17.75	0	0	0	0	0	0	9	2
18.5	18.25	0	0	0	0	0	0	4	0
19	18.75	0	0	0	0	3	3	5	2
19.5	19.25	0	0	0	0	0	0	6	0
20	19.75	0	0	0	0	1	1	2	2
20.5	20.25	0	0	0	0	0	0	1	0
21	20.75	0	0	0	0	0	0	3	0
21.5	21.25	0	0	0	0	0	0	2	0
22	21.75	0	0	0	0	0	0	2	0
22.5	22.25	0	0	0	0	0	0	2	3
23	22.75	0	0	0	0	0	0	2	0
23.5	23.25	0	0	0	0	0	0	2	0
24	23.75	0	0	0	0	0	0	0	1
24.5	24.25	0	0	0	0	0	0	3	0
25	24.75	0	0	0	0	0	0	3	0
25.5	25.25	0	0	0	0	0	0	1	0
26	25.75	0	0	0	0	0	0	1	0
26.5	26.25	0	0	0	0	0	0	0	0
27	26.75	0	0	0	0	0	0	1	0
27.5	27.25	0	0	0	0	0	0	1	0
28	27.75	0	0	0	0	0	0	2	0
28.5	28.25	0	0	0	0	0	0	2	0
29	28.75	0	0	0	0	0	0	0	0
29.5	29.25	0	0	0	0	0	0	2	0
30	29.75	0	0	0	0	0	0	2	0
30.5	30.25	0	0	0	0	0	0	2	0

Table 5. Baxter Interchange Phase 2 Stress Range Histogram Data Continued

RANGE	R_AVG	CH_1	CH_2	CH_3	CH_4	CH_5	CH_6	CH_7	CH_8
31	30.75	0	0	0	0	0	0	0	0
31.5	31.25	0	0	0	0	0	0	1	0
32	31.75	0	0	0	0	0	0	0	0
32.5	32.25	0	0	0	0	0	0	3	0
33	32.75	0	0	0	0	0	0	0	0
33.5	33.25	0	0	0	0	0	0	0	0
34	33.75	0	0	0	0	0	0	0	0
34.5	34.25	0	0	0	0	0	0	0	0
35	34.75	0	0	0	0	0	0	0	0
35.5	35.25	0	0	0	0	0	0	0	0
36	35.75	0	0	0	0	0	0	0	0
36.5	36.25	0	0	0	0	0	0	1	0
37	36.75	0	0	0	0	0	0	0	0
37.5	37.25	0	0	0	0	0	0	0	0
38	37.75	0	0	0	0	0	0	0	0
38.5	38.25	0	0	0	0	0	0	1	0
39	38.75	0	0	0	0	0	0	1	0
39.5	39.25	0	0	0	0	0	0	1	0
40	39.75	0	0	0	0	0	0	0	0
40.5	40.25	0	0	0	0	0	0	0	0
41	40.75	0	0	0	0	0	0	0	0
41.5	41.25	0	0	0	0	0	0	0	0
42	41.75	0	0	0	0	0	0	0	0
42.5	42.25	0	0	0	0	0	0	0	0
43	42.75	0	0	0	0	0	0	1	0
43.5	43.25	0	0	0	0	0	0	0	0
44	43.75	0	0	0	0	0	0	0	0
44.5	44.25	0	0	0	0	0	0	0	0
45	44.75	0	0	0	0	0	0	0	0
45.5	45.25	0	0	0	0	0	0	0	0
46	45.75	0	0	0	0	0	0	1	0
46.5	46.25	0	0	0	0	0	0	0	0
47	46.75	0	0	0	0	0	0	1	0
47.5	47.25	0	0	0	0	0	0	0	0
48	47.75	0	0	0	0	0	0	0	0
48.5	48.25	0	0	0	0	0	0	0	0
49	48.75	0	0	0	0	0	0	0	0
49.5	49.25	0	0	0	0	0	0	0	0
50	49.75	0	0	0	0	0	0	0	0
50.5	50.25	0	0	0	0	0	0	0	0
51	50.75	0	0	0	0	0	0	0	0
51.5	51.25	0	0	0	0	0	0	0	0
52	51.75	0	0	0	0	0	0	0	0
52.5	52.25	0	0	0	0	0	0	0	0
53	52.75	0	0	0	0	0	0	0	0
53.5	53.25	0	0	0	0	0	0	0	0
54	53.75	0	0	0	0	0	0	0	0
54.5	54.25	0	0	0	0	0	0	0	0
55	54.75	0	0	0	0	0	0	0	0
55.5	55.25	0	0	0	0	0	0	0	0
56	55.75	0	0	0	0	0	0	1	0
56.5	56.25	0	0	0	0	0	0	1	0
57	56.75	0	0	0	0	0	0	0	0
57.5	57.25	0	0	0	0	0	0	0	0
58	57.75	0	0	0	0	0	0	0	0
58.5	58.25	0	0	0	0	0	0	1	0
59	58.75	0	0	0	0	0	0	0	0
59.5	59.25	0	0	0	0	0	0	0	0
60	59.75	0	0	0	0	0	0	0	0
60.5	60.25	0	0	0	0	0	0	0	0
61	60.75	0	0	0	0	0	0	1	0
61.5	61.25	0	0	0	0	0	0	0	0
62	61.75	0	0	0	0	0	0	0	0

Table 5. Baxter Interchange Phase 2 Stress Range Histogram Data Continued

RANGE	R_AVG	CH_1	CH_2	CH_3	CH_4	CH_5	CH_6	CH_7	CH_8
62.5	62.25	0	0	0	0	0	0	0	0
63	62.75	0	0	0	0	0	0	0	0
63.5	63.25	0	0	0	0	0	0	0	0
64	63.75	0	0	0	0	0	0	0	0
64.5	64.25	0	0	0	0	0	0	0	0
65	64.75	0	0	0	0	0	0	0	0
65.5	65.25	0	0	0	0	0	0	0	0
66	65.75	0	0	0	0	0	0	0	0
66.5	66.25	0	0	0	0	0	0	0	0
67	66.75	0	0	0	0	0	0	0	0
67.5	67.25	0	0	0	0	0	0	0	0
68	67.75	0	0	0	0	0	0	0	0
68.5	68.25	0	0	0	0	0	0	0	0
69	68.75	0	0	0	0	0	0	0	0
69.5	69.25	0	0	0	0	0	0	0	0
70	69.75	0	0	0	0	0	0	0	0
70.5	70.25	0	0	0	0	0	0	0	0
71	70.75	0	0	0	0	0	0	0	0
71.5	71.25	0	0	0	0	0	0	0	0
72	71.75	0	0	0	0	0	0	0	0
72.5	72.25	0	0	0	0	0	0	0	0
73	72.75	0	0	0	0	0	0	0	0
73.5	73.25	0	0	0	0	0	0	0	0
74	73.75	0	0	0	0	0	0	0	0
74.5	74.25	0	0	0	0	0	0	0	0
75	74.75	0	0	0	0	0	0	1	0
75.5	75.25	0	0	0	0	0	0	0	0
76	75.75	0	0	0	0	0	0	0	0
76.5	76.25	0	0	0	0	0	0	0	0
77	76.75	0	0	0	0	0	0	0	0
77.5	77.25	0	0	0	0	0	0	0	0
78	77.75	0	0	0	0	0	0	0	0
78.5	78.25	0	0	0	0	0	0	0	0
79	78.75	0	0	0	0	0	0	0	0
79.5	79.25	0	0	0	0	0	0	0	0
80	79.75	0	0	0	0	0	0	0	0
S_{reff} (ksi)		**Unknown**	**1.67**	**1.69**	**1.60**	**1.59**	**1.62**	**1.72**	**1.60**
% Exceedance		Unknown	2.61%	4.44%	2.01%	2.72%	1.92%	3.60%	2.07%
Remaining Life		Uknown	65.6	46.8	54.8	54.6	67.1	83.1	56.6

Table 6. Buffalo Interchange Phase 2 Stress Range Histogram Data

RANGE	R_AVG	CH_1	CH_2	CH_3	CH_4	CH_5	CH_6	CH_7	CH_8
0.25	0	0	0	0	0	0	0	0	0
0.5	9989235	11684691	7442116	6060985	10356244	10465581	7255403	5495505	9989235
1	3853607	5134408	2921892	2419472	4116423	4199977	2817333	2156296	3853607
1.5	504205	652397	441946	468778	575394	439595	422816	398321	504205
2	90659	103633	103049	126956	107974	65550	98701	101902	90659
2.5	24285	25020	32057	40974	29365	16322	30168	31618	24285
`3	7959	8520	11928	15085	10153	5333	11459	11597	7959
3.5	3003	3411	5394	6733	3679	2187	5042	5006	3003
4	1172	1498	2496	3003	1573	1016	2384	2046	1172
4.5	497	802	1144	1343	662	497	1095	929	497
5	241	403	599	702	313	298	558	404	241
5.5	148	261	368	268	183	169	346	200	148
6	66	150	203	188	98	82	166	105	66
6.5	31	94	68	100	34	47	62	46	31
7	19	38	50	33	28	43	47	16	19
7.5	13	43	46	21	18	20	43	8	13
8	13	26	21	6	10	18	17	3	13
8.5	0	12	0	3	7	15	1	3	0
9	0	16	7	3	0	4	9	0	0
9.5	6	6	0	0	0	7	3	0	6
10	3	3	3	0	6	1	0	1	3
10.5	0	6	0	1	3	0	0	0	0
11	8	0	3	0	0	3	3	0	8
11.5	0	3	3	3	0	3	0	0	0
12	0	8	0	0	0	0	0	0	0
12.5	0	3	0	0	0	0	0	5	0
13	0	0	5	0	0	0	0	0	0
13.5	0	0	0	0	0	0	0	3	0
14	0	0	0	0	3	0	0	0	0
14.5	0	0	0	5	0	0	0	0	0
15	0	0	0	0	0	0	0	0	0
15.5	0	0	0	0	0	0	0	0	0
16	0	0	0	0	0	0	0	0	0
16.5	0	0	0	0	0	0	0	0	0
17	0	0	0	0	0	0	0	0	0
17.5	0	0	0	0	5	0	0	0	0
18	0	0	0	0	0	0	0	0	0
18.5	0	0	0	0	0	0	0	0	0
19	0	0	0	0	0	0	0	0	0
19.5	0	0	0	0	0	0	0	0	0
20	0	0	0	0	0	0	0	0	0
20.5	0	0	0	0	0	0	0	0	0
21	0	0	0	0	0	0	0	0	0
21.5	0	0	0	0	0	0	0	0	0
22	0	0	0	0	0	0	0	0	0
22.5	0	0	0	0	0	0	0	0	0
23	0	0	0	0	0	0	0	0	0
23.5	0	0	0	0	0	3	0	0	0
24	0	0	0	0	0	0	0	0	0
24.5	0	0	0	0	0	0	0	0	0
25	0	0	0	0	0	3	0	0	0
25.5	0	0	0	0	0	0	0	0	0
26	0	0	0	0	0	0	0	0	0
26.5	0	0	0	0	0	0	0	0	0
27	0	0	0	0	0	0	0	0	0
27.5	0	0	0	0	0	0	0	0	0
28	0	0	0	0	0	0	0	0	0
28.5	0	0	0	0	0	0	0	0	0
29	0	0	0	0	0	0	6	0	0
29.5	0	0	0	0	0	0	0	0	0
30	0	0	0	0	0	0	0	0	0
30.5	0	0	0	0	0	0	0	0	0

Table 6. Buffalo Interchange Phase 2 Stress Range Histogram Data Continued

RANGE	R_AVG	CH_1	CH_2	CH_3	CH_4	CH_5	CH_6	CH_7	CH_8
31	0	0	0	0	0	0	0	0	0
31.5	0	0	0	0	0	0	0	0	0
32	0	0	0	0	0	0	0	0	0
32.5	0	0	0	0	0	0	0	0	0
33	0	0	0	0	0	0	0	0	0
33.5	0	0	0	0	0	0	0	0	0
34	0	0	0	0	0	0	0	0	0
34.5	0	0	0	0	0	0	0	0	0
35	0	0	0	0	0	0	0	0	0
35.5	0	0	0	0	0	0	0	0	0
36	0	0	0	0	0	0	0	0	0
36.5	0	0	0	0	0	0	0	0	0
37	0	0	0	0	0	0	0	0	0
37.5	0	0	0	0	0	0	0	0	0
38	0	0	0	0	0	0	0	0	0
38.5	0	0	0	0	0	0	0	0	0
39	0	0	0	0	0	0	0	0	0
39.5	0	0	0	0	0	0	0	0	0
40	0	0	0	0	0	0	0	0	0
40.5	0	0	0	0	0	0	0	0	0
41	0	0	0	0	0	0	0	0	0
41.5	0	0	0	0	0	0	0	0	0
42	0	0	0	0	0	0	0	0	0
42.5	0	0	0	0	0	0	0	0	0
43	0	0	0	0	0	0	0	0	0
43.5	0	0	0	0	0	0	0	0	0
44	0	0	0	0	0	0	0	0	0
44.5	0	0	0	0	0	0	0	0	0
45	0	0	0	0	0	0	0	0	0
45.5	0	0	0	0	0	0	0	0	0
46	0	0	0	0	0	0	0	0	0
46.5	0	0	0	0	0	0	0	0	0
47	0	0	0	0	0	0	0	0	0
47.5	0	0	0	0	0	0	0	0	0
48	0	0	0	0	0	0	0	0	0
48.5	0	0	0	0	0	0	0	0	0
49	0	0	0	0	0	0	0	0	0
49.5	0	0	0	0	0	0	0	0	0
50	0	0	0	0	0	0	0	0	0
50.5	0	0	0	0	0	0	0	0	0
51	0	0	0	0	0	0	0	0	0
51.5	0	0	0	0	0	0	0	0	0
52	0	0	0	0	0	0	0	0	0
52.5	0	0	0	0	0	0	0	0	0
53	0	0	0	0	0	0	0	0	0
53.5	0	0	0	0	0	0	0	0	0
54	0	0	0	0	0	0	0	0	0
54.5	0	0	0	0	0	0	0	0	0
55	0	0	0	0	0	0	0	0	0
55.5	0	0	0	0	0	0	0	0	0
56	0	0	0	0	0	0	0	0	0
56.5	0	0	0	0	0	0	0	0	0
57	0	0	0	0	0	0	0	0	0
57.5	0	0	0	0	0	0	0	0	0
58	0	0	0	0	0	0	0	0	0
58.5	0	0	0	0	0	0	0	0	0
59	0	0	0	0	0	0	0	0	0
59.5	0	0	0	0	0	0	0	0	0
60	0	0	0	0	0	0	0	0	0
60.5	0	0	0	0	0	0	0	0	0
61	0	0	0	0	0	0	0	0	0
61.5	0	0	0	0	0	0	0	0	0
62	0	0	0	0	0	0	0	0	0

Table 6. Buffalo Interchange Phase 2 Stress Range Histogram Data Continued

RANGE	R_AVG	CH_1	CH_2	CH_3	CH_4	CH_5	CH_6	CH_7	CH_8
62.5	0	0	0	0	0	0	0	0	0
63	0	0	0	0	0	0	0	0	0
63.5	0	0	0	0	0	0	0	0	0
64	0	0	0	0	0	0	0	0	0
64.5	0	0	0	0	0	0	0	0	0
65	0	0	0	0	0	0	0	0	0
65.5	0	0	0	0	0	0	0	0	0
66	0	0	0	0	0	0	0	0	0
66.5	0	0	0	0	0	0	0	0	0
67	0	0	0	0	0	0	0	0	0
67.5	0	0	0	0	0	0	0	0	0
68	0	0	0	0	0	0	0	0	0
68.5	0	0	0	0	0	0	0	0	0
69	0	0	0	0	0	0	0	0	0
69.5	0	0	0	0	0	0	0	0	0
70	0	0	0	0	0	0	0	0	0
70.5	0	0	0	0	0	0	0	0	0
71	0	0	0	0	0	0	0	0	0
71.5	0	0	0	0	0	0	0	0	0
72	0	0	0	0	0	0	0	0	0
72.5	0	0	0	0	0	0	0	0	0
73	0	0	0	0	0	0	0	0	0
73.5	0	0	0	0	0	0	0	0	0
74	0	0	0	0	0	0	0	0	0
74.5	0	0	0	0	0	0	0	0	0
75	0	0	0	0	0	0	0	0	0
75.5	0	0	0	0	0	0	0	0	0
76	0	0	0	0	0	0	0	0	0
76.5	0	0	0	0	0	0	0	0	0
77	0	0	0	0	0	0	0	0	0
77.5	0	0	0	0	0	0	0	0	0
78	0	0	0	0	0	0	0	0	0
78.5	0	0	0	0	0	0	0	0	0
79	0	0	0	0	0	0	0	0	0
79.5	0	0	0	0	0	0	0	0	0
80	0	0	0	0	0	0	0	0	0
S_{reff} (ksi)		**1.54**	**1.51**	**1.59**	**1.62**	**1.55**	**1.50**	**1.59**	**1.61**
% Exceedance		2.08%	1.92%	3.73%	4.14%	2.30%	1.83%	3.71%	3.69%
Remaining Life		>100	>100	>100	>100	>100	>100	>100	>100

Table 7. Dwyer Junction Phase 2 Stress Range Histogram Data

RANGE	R_AVG	CH_1	CH_2	CH_3	CH_4	CH_5	CH_6	CH_7	CH_8
0.25	0	0	0	0	0	0	0	0	0
0.5	0.375	26773655	18679337	22309250	25714911	23750601	28337731	22350530	29303096
1	0.75	10556492	6062866	8447319	9616324	8958625	10243434	9508260	11197867
1.5	1.25	2756377	1498013	1877014	2137669	2226509	2627831	2380123	2411614
2	1.75	1173030	934311	994013	1126612	1196707	1103865	851355	1242881
2.5	2.25	511849	267690	408289	395638	461962	432041	284709	474720
3	2.75	264602	95489	140354	171253	203502	195417	123076	217066
3.5	3.25	130384	41723	63504	77590	92233	90521	55907	101877
4	3.75	63822	16812	28639	35143	41596	45276	25721	48430
4.5	4.25	31921	6487	13210	16431	18587	22970	12781	23300
5	4.75	15508	3019	5764	7323	8548	11408	7579	11319
5.5	5.25	7426	877	2636	3344	4054	6928	3944	5346
6	5.75	3722	345	1284	1635	1867	5570	1954	2555
6.5	6.25	1791	158	823	672	1137	4216	1009	1143
7	6.75	1279	39	434	342	389	2722	765	517
7.5	7.25	817	6	208	136	138	1961	578	292
8	7.75	227	30	43	94	74	1365	387	120
8.5	8.25	91	26	38	90	43	1155	199	36
9	8.75	68	24	45	90	15	687	56	42
9.5	9.25	24	0	19	201	19	356	31	10
10	9.75	6	19	1	340	12	209	23	16
10.5	10.25	19	12	6	163	10	216	12	23
11	10.75	18	0	30	68	12	56	13	16
11.5	11.25	0	18	6	37	6	76	0	14
12	11.75	6	6	20	42	12	24	12	25
12.5	12.25	12	12	6	33	19	18	1	7
13	12.75	6	22	0	39	0	6	24	18
13.5	13.25	6	6	6	50	18	10	6	30
14	13.75	18	6	6	52	18	10	6	43
14.5	14.25	6	6	0	97	0	12	6	78
15	14.75	12	6	15	79	12	7	0	48
15.5	15.25	18	6	6	26	12	12	12	48
16	15.75	6	6	0	40	0	26	0	30
16.5	16.25	6	6	6	42	12	6	12	42
17	16.75	6	6	13	55	6	8	0	30
17.5	17.25	1	6	11	56	18	8	12	60
18	17.75	12	6	6	45	18	0	0	72
18.5	18.25	6	6	6	18	6	6	6	12
19	18.75	6	6	12	13	18	2	0	6
19.5	19.25	28	6	6	14	18	14	12	12
20	19.75	14	12	6	7	6	0	6	6
20.5	20.25	12	12	6	0	6	12	0	0
21	20.75	0	6	0	7	24	32	12	0
21.5	21.25	12	6	12	2	24	20	0	0
22	21.75	12	18	0	11	78	20	6	0
22.5	22.25	18	12	6	0	78	2	0	0
23	22.75	12	18	0	0	48	28	6	0
23.5	23.25	6	18	6	1	12	18	12	0
24	23.75	12	54	6	1	24	20	0	0
24.5	24.25	6	72	6	0	6	8	6	0
25	24.75	54	60	0	0	42	8	0	0
25.5	25.25	66	24	6	0	24	6	0	0
26	25.75	66	36	0	0	24	12	12	0
26.5	26.25	48	36	6	1	42	0	0	0
27	26.75	12	18	6	0	42	0	6	0
27.5	27.25	6	30	6	0	24	12	0	0
28	27.75	12	12	0	0	6	0	6	10
28.5	28.25	24	42	6	0	12	6	6	0
29	28.75	24	90	6	0	0	2	0	0
29.5	29.25	24	36	6	0	0	6	6	2
30	29.75	18	24	0	0	0	0	0	1
30.5	30.25	30	0	18	0	0	6	12	0

Table 7. Dwyer Junction Phase 2 Stress Range Histogram Data Continued

RANGE	R_AVG	CH_1	CH_2	CH_3	CH_4	CH_5	CH_6	CH_7	CH_8
31	30.75	48	6	6	0	0	8	0	0
31.5	31.25	36	0	6	0	0	0	0	0
32	31.75	0	0	6	0	0	0	12	0
32.5	32.25	6	0	6	0	6	6	0	0
33	32.75	18	0	6	0	0	6	6	0
33.5	33.25	0	0	6	0	0	0	0	0
34	33.75	12	0	0	0	0	0	12	0
34.5	34.25	0	0	30	0	0	6	0	0
35	34.75	0	0	24	0	0	6	6	0
35.5	35.25	0	0	24	0	0	0	0	0
36	35.75	0	0	12	0	0	8	6	0
36.5	36.25	0	0	0	0	0	0	6	0
37	36.75	0	0	0	0	0	0	18	0
37.5	37.25	0	0	12	0	0	12	18	0
38	37.75	0	0	12	0	0	8	0	0
38.5	38.25	0	0	18	0	0	6	12	0
39	38.75	0	0	6	0	0	0	18	0
39.5	39.25	0	0	12	0	0	12	0	0
40	39.75	0	0	6	0	0	12	0	0
40.5	40.25	0	0	12	0	0	6	6	0
41	40.75	0	0	6	0	0	12	12	0
41.5	41.25	0	0	42	0	0	6	36	0
42	41.75	0	0	24	0	0	6	42	0
42.5	42.25	0	0	30	0	0	6	30	0
43	42.75	0	0	12	0	0	6	48	0
43.5	43.25	0	0	30	0	0	6	12	0
44	43.75	0	0	6	0	0	6	12	0
44.5	44.25	0	0	30	0	0	0	6	0
45	44.75	0	0	12	0	0	12	18	0
45.5	45.25	0	0	30	0	0	12	12	0
46	45.75	0	0	36	0	0	24	12	0
46.5	46.25	0	0	36	0	0	60	18	0
47	46.75	0	0	18	0	0	42	12	0
47.5	47.25	0	0	18	0	0	18	12	0
48	47.75	0	0	18	0	0	18	12	0
48.5	48.25	0	0	18	0	0	6	18	0
49	48.75	0	0	12	0	0	6	12	0
49.5	49.25	0	0	0	0	0	24	24	0
50	49.75	0	0	0	0	0	24	36	0
50.5	50.25	0	0	0	0	0	18	30	0
51	50.75	0	0	0	0	0	6	36	0
51.5	51.25	0	0	0	0	0	6	12	0
52	51.75	0	0	0	0	0	6	18	0
52.5	52.25	0	0	0	0	0	6	12	0
53	52.75	0	0	0	0	0	12	0	0
53.5	53.25	0	0	0	0	0	6	0	0
54	53.75	0	0	0	0	0	12	0	0
54.5	54.25	0	0	0	0	0	18	0	0
55	54.75	0	0	0	0	0	36	0	0
55.5	55.25	0	0	0	0	0	42	0	0
56	55.75	0	0	0	0	0	24	0	0
56.5	56.25	0	0	0	0	0	30	0	0
57	56.75	0	0	0	0	0	12	6	0
57.5	57.25	0	0	0	0	0	6	0	0
58	57.75	0	0	0	0	0	0	0	0
58.5	58.25	0	0	0	0	0	0	0	0
59	58.75	0	0	0	0	0	0	0	0
59.5	59.25	0	0	0	0	0	0	0	0
60	59.75	0	0	0	0	0	0	0	0
60.5	60.25	0	0	0	0	0	0	0	0
61	60.75	0	0	0	0	0	0	0	0
61.5	61.25	0	0	0	0	0	0	0	0
62	61.75	0	0	0	0	0	0	0	0

Table 7. Dwyer Junction Phase 2 Stress Range Histogram Data Continued

RANGE	R_AVG	CH_1	CH_2	CH_3	CH_4	CH_5	CH_6	CH_7	CH_8
62.5	62.25	0	0	0	0	0	0	0	0
63	62.75	0	0	0	0	0	6	0	0
63.5	63.25	0	0	0	0	0	0	0	0
64	63.75	0	0	0	0	0	0	0	0
64.5	64.25	0	0	0	0	0	0	0	0
65	64.75	0	0	0	0	0	0	0	0
65.5	65.25	0	0	0	0	0	0	0	0
66	65.75	0	0	0	0	0	0	0	0
66.5	66.25	0	0	0	0	0	0	0	0
67	66.75	0	0	0	0	0	0	0	0
67.5	67.25	0	0	0	0	0	0	0	0
68	67.75	0	0	0	0	0	0	0	0
68.5	68.25	0	0	0	0	0	0	0	0
69	68.75	0	0	0	0	0	0	0	0
69.5	69.25	0	0	0	0	0	0	0	0
70	69.75	0	0	0	0	0	0	0	0
70.5	70.25	0	0	0	0	0	0	0	0
71	70.75	0	0	0	0	0	0	0	0
71.5	71.25	0	0	0	0	0	0	0	0
72	71.75	0	0	0	0	0	0	0	0
72.5	72.25	0	0	0	0	0	0	0	0
73	72.75	0	0	0	0	0	0	0	0
73.5	73.25	0	0	0	0	0	0	0	0
74	73.75	0	0	0	0	0	0	0	0
74.5	74.25	0	0	0	0	0	0	0	0
75	74.75	0	0	0	0	0	0	0	0
75.5	75.25	0	0	0	0	0	0	0	0
76	75.75	0	0	0	0	0	0	0	0
76.5	76.25	0	0	0	0	0	0	0	0
77	76.75	0	0	0	0	0	0	0	0
77.5	77.25	0	0	0	0	0	0	0	0
78	77.75	0	0	0	0	0	0	0	0
78.5	78.25	0	0	0	0	0	0	0	0
79	78.75	0	0	0	0	0	0	0	0
79.5	79.25	0	0	0	0	0	0	0	0
80	79.75	0	0	0	0	0	0	0	0
S_{reff} (ksi)		**1.77**	**1.76**	**1.78**	**1.77**	**1.79**	**1.74**	**1.69**	**1.78**
% Exceedance		10.51%	5.76%	7.27%	7.93%	8.74%	8.59%	6.24%	9.08%
Remaining Life		10.8	26.1	18.5	15.9	13.4	13.7	21.3	12.4

Table 8. Vedauwoo Interchange Phase 2 Stress Range Histogram Data

RANGE	R_AVG	CH_1	CH_2	CH_3	CH_4	CH_5	CH_6	CH_7	CH_8
0.25	0	0	0	0	0	0	0	0	0
0.5	0.375	58269189	61639973	49062339	49094060	35057150	64387672	47839693	48967692
1	0.75	17643216	21368155	19133268	15652280	10649720	21914492	19260722	18177482
1.5	1.25	4922653	4921693	4836334	4118480	2932701	4739086	4798490	4191604
2	1.75	2426035	2437176	2060800	1604773	1560558	2363890	1966577	1459207
2.5	2.25	1114988	1230092	860712	581374	773611	1308878	822908	607754
`3	2.75	511533	623230	345740	204166	356585	652613	316294	260593
3.5	3.25	238580	312952	137814	72141	169788	318578	120571	94108
4	3.75	109231	148905	58463	24986	80119	155683	50424	32893
4.5	4.25	46677	69521	24945	8235	35855	73374	21060	11549
5	4.75	21017	32953	11497	2994	16830	35574	9203	4378
5.5	5.25	9479	15132	5172	1132	7515	16106	4376	1474
6	5.75	4469	7773	2668	433	3819	8904	1885	464
6.5	6.25	2304	4538	1207	142	1874	4943	878	201
7	6.75	1181	2723	792	45	917	2981	310	79
7.5	7.25	729	1955	225	43	545	1885	164	18
8	7.75	554	1198	148	5	313	1196	136	7
8.5	8.25	274	783	129	0	170	775	147	7
9	8.75	254	577	108	0	66	537	107	0
9.5	9.25	234	421	136	0	15	425	186	0
10	9.75	181	269	112	1	15	244	212	0
10.5	10.25	134	109	212	0	1	145	172	0
11	10.75	44	85	204	1	5	125	106	0
11.5	11.25	28	118	92	0	0	94	89	0
12	11.75	4	64	84	0	0	60	74	0
12.5	12.25	0	96	68	0	0	126	44	0
13	12.75	0	144	66	0	0	160	40	0
13.5	13.25	2	185	28	0	0	97	30	1
14	13.75	2	116	16	1	0	104	9	0
14.5	14.25	2	80	6	0	0	84	1	0
15	14.75	0	68	1	0	0	65	0	0
15.5	15.25	0	64	0	0	0	76	1	0
16	15.75	0	46	0	2	0	39	1	0
16.5	16.25	0	22	2	0	0	44	0	0
17	16.75	4	6	0	0	0	8	1	1
17.5	17.25	2	1	1	0	0	0	0	0
18	17.75	0	1	1	0	0	0	2	0
18.5	18.25	0	0	1	0	0	0	0	0
19	18.75	0	3	3	2	0	0	0	0
19.5	19.25	1	0	1	1	0	0	0	0
20	19.75	0	0	0	3	0	0	1	0
20.5	20.25	1	0	1	1	0	0	0	0
21	20.75	0	1	0	0	0	0	0	0
21.5	21.25	0	0	1	0	0	1	0	0
22	21.75	0	0	1	1	0	0	0	1
22.5	22.25	0	0	1	1	0	0	0	0
23	22.75	1	0	0	0	0	0	0	0
23.5	23.25	0	0	0	0	0	0	0	0
24	23.75	0	0	0	0	0	0	1	0
24.5	24.25	0	1	2	0	0	0	0	0
25	24.75	0	1	2	1	0	0	0	0
25.5	25.25	1	0	0	1	0	0	1	0
26	25.75	0	0	15	0	1	0	1	0
26.5	26.25	1	1	0	1	0	1	0	0
27	26.75	0	0	0	1	0	0	0	0
27.5	27.25	0	0	0	0	0	0	2	2
28	27.75	0	1	0	0	0	0	2	0
28.5	28.25	0	0	0	0	0	0	0	0
29	28.75	1	0	0	1	0	0	2	0
29.5	29.25	0	0	0	1	0	0	2	1
30	29.75	0	0	0	15	0	0	1	0
30.5	30.25	0	0	0	1	0	0	4	0

Table 8. Vedauwoo Interchange Phase 2 Stress Range Histogram Data Continued

RANGE	R_AVG	CH_1	CH_2	CH_3	CH_4	CH_5	CH_6	CH_7	CH_8
31	30.75	0	0	0	1	0	0	0	0
31.5	31.25	0	0	0	0	0	0	11	0
32	31.75	1	0	0	0	0	0	0	0
32.5	32.25	0	0	0	0	0	0	0	0
33	32.75	0	0	0	0	0	0	0	0
33.5	33.25	0	0	0	0	0	1	0	0
34	33.75	0	0	0	0	0	0	0	0
34.5	34.25	0	0	0	0	0	0	0	0
35	34.75	0	0	0	0	0	0	0	2
35.5	35.25	0	0	0	1	0	2	2	0
36	35.75	0	0	2	0	0	0	0	0
36.5	36.25	0	0	0	0	0	0	0	0
37	36.75	0	0	0	0	0	0	0	0
37.5	37.25	0	0	0	0	0	0	0	0
38	37.75	0	0	3	1	0	0	0	0
38.5	38.25	0	0	0	0	0	0	0	0
39	38.75	0	0	0	0	0	0	0	0
39.5	39.25	0	1	0	0	0	0	0	0
40	39.75	0	2	0	0	0	0	0	0
40.5	40.25	2	0	0	0	0	2	0	0
41	40.75	0	0	0	2	0	0	0	1
41.5	41.25	0	1	0	0	0	0	0	0
42	41.75	0	4	0	0	0	0	0	2
42.5	42.25	1	11	0	0	0	0	0	0
43	42.75	0	0	2	2	0	0	0	11
43.5	43.25	0	0	0	0	0	0	0	0
44	43.75	0	0	0	0	0	0	0	4
44.5	44.25	0	0	0	0	0	0	0	0
45	44.75	0	0	0	0	1	0	0	0
45.5	45.25	0	0	0	0	0	0	2	0
46	45.75	0	0	2	0	0	0	0	0
46.5	46.25	0	0	0	0	1	0	0	0
47	46.75	0	0	1	0	10	0	0	0
47.5	47.25	0	0	0	0	0	0	0	0
48	47.75	0	0	0	2	0	0	0	0
48.5	48.25	0	0	0	0	0	0	0	0
49	48.75	0	0	0	0	0	0	0	1
49.5	49.25	0	0	0	0	0	2	0	0
50	49.75	0	0	2	0	0	0	2	0
50.5	50.25	0	0	0	0	0	0	0	0
51	50.75	1	0	0	0	0	0	0	0
51.5	51.25	0	0	0	0	0	0	0	0
52	51.75	0	0	0	0	0	0	0	0
52.5	52.25	0	0	0	0	0	0	0	0
53	52.75	0	0	0	0	0	0	0	0
53.5	53.25	0	0	0	0	0	0	0	0
54	53.75	0	0	0	0	0	0	0	0
54.5	54.25	0	0	0	0	0	0	0	0
55	54.75	0	0	0	0	0	0	0	0
55.5	55.25	0	0	0	0	0	0	0	0
56	55.75	0	0	0	0	0	0	0	0
56.5	56.25	0	0	0	0	0	0	0	0
57	56.75	0	0	0	0	0	0	0	0
57.5	57.25	0	0	0	0	0	0	0	0
58	57.75	0	0	0	0	0	0	0	0
58.5	58.25	0	0	0	0	0	0	0	0
59	58.75	0	0	0	0	0	0	0	0
59.5	59.25	0	0	0	0	0	0	0	0
60	59.75	0	0	0	0	0	0	0	0
60.5	60.25	0	0	0	0	0	0	0	0
61	60.75	0	0	0	0	0	0	0	0
61.5	61.25	0	0	0	0	0	0	0	0
62	61.75	0	0	0	0	0	0	0	0

Table 8. Vedauwoo Interchange Phase 2 Stress Range Histogram Data Continued

RANGE	R_AVG	CH_1	CH_2	CH_3	CH_4	CH_5	CH_6	CH_7	CH_8
62.5	62.25	0	0	0	0	0	0	0	0
63	62.75	0	0	0	0	0	0	0	0
63.5	63.25	0	0	0	0	0	0	0	0
64	63.75	0	0	0	0	0	0	0	0
64.5	64.25	0	0	0	0	0	0	0	0
65	64.75	0	0	0	0	0	0	0	0
65.5	65.25	0	0	0	0	0	0	0	0
66	65.75	0	0	0	0	0	0	0	0
66.5	66.25	0	0	0	0	0	0	0	0
67	66.75	0	0	0	0	0	0	0	0
67.5	67.25	0	0	0	0	0	0	0	0
68	67.75	0	0	0	0	1	0	0	0
68.5	68.25	0	0	0	0	0	0	0	0
69	68.75	0	0	0	0	0	0	0	0
69.5	69.25	0	0	0	0	0	0	0	0
70	69.75	0	0	0	0	0	0	0	0
70.5	70.25	0	0	0	0	0	0	0	0
71	70.75	0	0	0	0	0	0	0	0
71.5	71.25	0	0	0	0	0	0	0	0
72	71.75	0	0	0	0	0	0	0	0
72.5	72.25	0	0	0	0	0	0	0	0
73	72.75	0	0	0	0	0	0	0	0
73.5	73.25	0	0	0	0	0	0	0	0
74	73.75	0	0	0	0	0	0	0	0
74.5	74.25	0	0	0	0	0	0	0	0
75	74.75	0	0	0	0	0	0	0	0
75.5	75.25	0	0	0	0	0	0	0	0
76	75.75	0	0	0	0	0	0	0	0
76.5	76.25	0	0	0	0	0	0	0	0
77	76.75	0	0	0	0	0	0	0	0
77.5	77.25	0	0	0	0	0	0	0	0
78	77.75	0	0	0	0	0	0	0	0
78.5	78.25	0	2	0	0	0	0	0	0
79	78.75	0	0	0	0	0	0	0	0
79.5	79.25	0	0	0	0	0	0	0	0
80	79.75	0	0	0	0	0	0	0	0
S_{reff} (ksi)		**1.80**	**1.82**	**1.75**	**1.71**	**1.83**	**1.84**	**1.74**	**1.72**
% Exceedance		10.06%	12.47%	7.07%	4.75%	11.35%	13.16%	6.49%	6.09%
Remaining Life		-8.0	-8.7	-5.7	-1.3	-2.8	-8.9	-5.2	-1.8

APPENDIX B – COMBINED STRESS RANGE HISTOGRAM DATA FOR PHASE 1 AND PHASE 2 MONITORING

Table 9. Baxter Interchange Combined Phases Stress Range Histogram Data

RANGE	R_AVG	CH_1	CH_2	CH_3	CH_4	CH_5	CH_6	CH_7	CH_8
0.25	0	0	0	0	0	0	0	0	0
0.5	0.375	3127853	33230571	26859926	42432856	47603834	36856315	14192337	41332384
1	0.75	1334288	11675725	10172616	14761384	17477510	11751614	5222532	14050422
1.5	1.25	165465	1706008	2014325	2203598	2460156	1689801	1007860	2087793
2	1.75	19668	582340	700672	570549	534853	495849	445793	560612
2.5	2.25	3357	153016	244067	138007	138182	119489	122502	135474
`3	2.75	891	40975	88368	35761	43566	31606	32830	35109
3.5	3.25	287	12009	33405	10636	14067	6044	9296	9723
4	3.75	103	2694	12362	3779	5080	1356	3603	3376
4.5	4.25	38	734	3140	1500	2193	375	2196	1343
5	4.75	13	227	564	597	1090	107	641	646
5.5	5.25	3	64	33	212	566	42	317	282
6	5.75	5	39	7	91	391	15	179	168
6.5	6.25	2	19	0	62	264	22	127	110
7	6.75	0	16	1	35	208	27	130	85
7.5	7.25	2	24	0	40	189	19	114	49
8	7.75	2	19	0	15	170	15	49	53
8.5	8.25	1	17	0	2	154	8	30	72
9	8.75	0	10	0	4	130	18	38	75
9.5	9.25	0	13	0	1	129	19	41	124
10	9.75	0	17	0	2	108	28	31	177
10.5	10.25	0	17	0	0	109	10	17	143
11	10.75	0	24	0	1	96	10	19	63
11.5	11.25	0	6	0	0	76	13	11	40
12	11.75	0	12	0	0	84	7	12	37
12.5	12.25	0	12	0	0	76	0	10	49
13	12.75	0	6	0	0	81	0	9	69
13.5	13.25	0	1	2	0	73	4	7	69
14	13.75	0	0	0	0	55	0	10	84
14.5	14.25	0	0	5	0	64	5	5	38
15	14.75	0	0	1	1	32	0	9	33
15.5	15.25	0	0	4	0	45	1	4	32
16	15.75	0	0	0	0	42	0	4	33
16.5	16.25	0	0	0	0	29	0	7	0
17	16.75	0	0	0	0	31	0	1	2
17.5	17.25	0	0	0	0	22	0	4	0
18	17.75	0	0	0	0	9	0	9	2
18.5	18.25	0	0	0	0	14	0	4	0
19	18.75	0	0	0	0	17	3	5	2
19.5	19.25	0	0	0	0	20	0	6	0
20	19.75	0	0	0	0	16	1	2	2
20.5	20.25	0	0	0	0	17	0	1	0
21	20.75	0	0	0	0	17	0	3	0
21.5	21.25	0	0	0	0	20	0	2	0
22	21.75	0	0	0	0	17	0	2	0
22.5	22.25	0	0	0	0	24	0	2	3
23	22.75	0	0	0	0	19	0	1	0
23.5	23.25	0	0	0	0	8	0	2	0
24	23.75	0	0	0	0	12	0	0	1
24.5	24.25	0	0	0	0	14	0	3	0
25	24.75	0	0	0	0	9	0	1	0
25.5	25.25	0	0	0	0	3	0	1	0
26	25.75	0	0	0	0	14	0	1	0
26.5	26.25	0	0	0	0	16	0	0	0
27	26.75	0	0	0	0	8	0	1	0
27.5	27.25	0	0	0	0	5	0	1	0
28	27.75	0	0	0	0	10	0	2	0
28.5	28.25	0	0	0	0	6	0	2	0
29	28.75	0	0	0	0	14	0	0	0
29.5	29.25	0	0	0	0	8	0	2	0
30	29.75	0	0	0	0	5	0	2	0
30.5	30.25	0	0	0	0	13	0	1	0

Table 9. Baxter Interchange Combined Phases Stress Range Histogram Data Continued

RANGE	R_AVG	CH_1	CH_2	CH_3	CH_4	CH_5	CH_6	CH_7	CH_8
31	30.75	0	0	0	0	10	0	0	0
31.5	31.25	0	0	0	0	3	0	1	0
32	31.75	0	0	0	0	5	0	0	0
32.5	32.25	0	0	0	0	3	0	1	0
33	32.75	0	0	0	0	6	0	0	0
33.5	33.25	0	0	0	0	5	0	0	0
34	33.75	0	0	0	0	5	0	0	0
34.5	34.25	0	0	0	0	10	0	0	0
35	34.75	0	0	0	0	4	0	0	0
35.5	35.25	0	0	0	0	4	0	0	0
36	35.75	0	0	0	0	5	0	0	0
36.5	36.25	0	0	0	0	6	0	1	0
37	36.75	0	0	0	0	2	0	0	0
37.5	37.25	0	0	0	0	4	0	0	0
38	37.75	0	0	0	0	3	0	0	0
38.5	38.25	0	0	0	0	2	0	1	0
39	38.75	0	0	0	0	2	0	1	0
39.5	39.25	0	0	0	0	10	0	0	0
40	39.75	0	0	0	0	3	0	0	0
40.5	40.25	0	0	0	0	0	0	0	0
41	40.75	0	0	0	0	2	0	0	0
41.5	41.25	0	0	0	0	3	0	0	0
42	41.75	0	0	0	0	2	0	0	0
42.5	42.25	0	0	0	0	5	0	0	0
43	42.75	0	0	0	0	2	0	0	0
43.5	43.25	0	0	0	0	4	0	0	0
44	43.75	0	0	0	0	9	0	0	0
44.5	44.25	0	0	0	0	2	0	0	0
45	44.75	0	0	0	0	4	0	0	0
45.5	45.25	0	0	0	0	1	0	0	0
46	45.75	0	0	0	0	0	0	1	0
46.5	46.25	0	0	0	0	2	0	0	0
47	46.75	0	0	0	0	4	0	1	0
47.5	47.25	0	0	0	0	3	0	0	0
48	47.75	0	0	0	0	1	0	0	0
48.5	48.25	0	0	0	0	2	0	0	0
49	48.75	0	0	0	0	3	0	0	0
49.5	49.25	0	0	0	0	0	0	0	0
50	49.75	0	0	0	0	2	0	0	0
50.5	50.25	0	0	0	0	0	0	0	0
51	50.75	0	0	0	0	0	0	0	0
51.5	51.25	0	0	0	0	1	0	0	0
52	51.75	0	0	0	0	3	0	0	0
52.5	52.25	0	0	0	0	2	0	0	0
53	52.75	0	0	0	0	2	0	0	0
53.5	53.25	0	0	0	0	3	0	0	0
54	53.75	0	0	0	0	0	0	0	0
54.5	54.25	0	0	0	0	2	0	0	0
55	54.75	0	0	0	0	2	0	0	0
55.5	55.25	0	0	0	0	1	0	0	0
56	55.75	0	0	0	0	3	0	1	0
56.5	56.25	0	0	0	0	0	0	1	0
57	56.75	0	0	0	0	0	0	0	0
57.5	57.25	0	0	0	0	0	0	0	0
58	57.75	0	0	0	0	1	0	0	0
58.5	58.25	0	0	0	0	0	0	1	0
59	58.75	0	0	0	0	2	0	0	0
59.5	59.25	0	0	0	0	2	0	0	0
60	59.75	0	0	0	0	1	0	0	0
60.5	60.25	0	0	0	0	1	0	0	0
61	60.75	0	0	0	0	0	0	1	0
61.5	61.25	0	0	0	0	0	0	0	0
62	61.75	0	0	0	0	1	0	0	0

Table 9. Baxter Interchange Combined Phases Stress Range Histogram Data Continued

RANGE	R_AVG	CH_1	CH_2	CH_3	CH_4	CH_5	CH_6	CH_7	CH_8
62.5	62.25	0	0	0	0	1	0	0	0
63	62.75	0	0	0	0	3	0	0	0
63.5	63.25	0	0	0	0	0	0	0	0
64	63.75	0	0	0	0	0	0	0	0
64.5	64.25	0	0	0	0	0	0	0	0
65	64.75	0	0	0	0	0	0	0	0
65.5	65.25	0	0	0	0	2	0	0	0
66	65.75	0	0	0	0	0	0	1	0
66.5	66.25	0	0	0	0	0	0	0	0
67	66.75	0	0	0	0	0	0	0	0
67.5	67.25	0	0	0	0	0	0	0	0
68	67.75	0	0	0	0	1	0	0	0
68.5	68.25	0	0	0	0	1	0	0	0
69	68.75	0	0	0	0	0	0	0	0
69.5	69.25	0	0	0	0	0	0	0	0
70	69.75	0	0	0	0	1	0	0	0
70.5	70.25	0	0	0	0	1	0	0	0
71	70.75	0	0	0	0	0	0	0	0
71.5	71.25	0	0	0	0	0	0	0	0
72	71.75	0	0	0	0	1	0	0	0
72.5	72.25	0	0	0	0	1	0	0	0
73	72.75	0	0	0	0	1	0	0	0
73.5	73.25	0	0	0	0	3	0	0	0
74	73.75	0	0	0	0	0	0	0	0
74.5	74.25	0	0	0	0	0	0	0	0
75	74.75	0	0	0	0	1	0	1	0
75.5	75.25	0	0	0	0	0	0	0	0
76	75.75	0	0	0	0	0	0	0	0
76.5	76.25	0	0	0	0	1	0	0	0
77	76.75	0	0	0	0	1	0	0	0
77.5	77.25	0	0	0	0	0	0	0	0
78	77.75	0	0	0	0	0	0	0	0
78.5	78.25	0	0	0	0	1	0	0	0
79	78.75	0	0	0	0	0	0	0	0
79.5	79.25	0	0	0	0	1	0	0	0
80	79.75	0	0	0	0	0	0	0	0
S_{reff} (ksi)		**1.45**	**1.63**	**1.68**	**1.58**	**1.56**	**1.60**	**1.68**	**1.58**
% Exceedance		0.71%	2.28%	4.45%	1.78%	2.16%	1.70%	3.06%	1.84%
Remaining Life		>100	>100	86.7	>100	>100	>100	>100	>100

Table 10. Buffalo Interchange Combined Phases Stress Range Histogram Data

RANGE	R_AVG	CH_1	CH_2	CH_3	CH_4	CH_5	CH_6	CH_7	CH_8
0.25	0	0	0	0	0	0	0	0	0
0.5	19736742	23286368	14533012	11742708	20551090	20809792	14176024	10599281	19736742
1	7267843	9853737	5407389	4505836	7819609	8023872	5227966	3994973	7267843
1.5	910917	1201510	771483	821516	1050108	805434	741492	691958	910917
2	156949	182382	170110	208641	189985	113332	163365	165566	156949
2.5	39074	41098	51261	65190	48358	26325	48411	50387	39074
`3	12426	13325	18611	24076	15865	8161	18008	18455	12426
3.5	4566	5077	8338	10559	5678	3284	7851	7788	4566
4	1723	2199	3693	4567	2402	1452	3556	3198	1723
4.5	686	1150	1681	2097	974	751	1610	1345	686
5	306	576	864	991	418	410	809	593	306
5.5	198	351	505	397	237	224	475	264	198
6	77	183	264	243	126	105	227	149	77
6.5	38	127	104	138	45	65	97	49	38
7	24	51	65	42	38	49	60	18	24
7.5	17	43	51	23	19	31	52	8	17
8	14	34	29	6	14	18	21	3	14
8.5	0	12	0	3	8	21	2	3	0
9	0	20	8	3	0	5	9	0	0
9.5	6	7	0	0	0	8	3	0	6
10	4	3	3	0	6	2	0	2	4
10.5	0	6	0	2	3	0	0	0	0
11	8	1	4	1	0	3	3	0	8
11.5	0	3	3	3	0	3	0	1	0
12	0	8	0	0	0	0	0	0	0
12.5	0	3	0	0	0	0	0	5	0
13	0	0	5	0	0	0	0	0	0
13.5	0	0	0	0	1	0	0	3	0
14	0	0	0	0	3	0	0	0	0
14.5	0	0	0	5	0	0	0	0	0
15	0	0	0	0	0	0	0	0	0
15.5	0	0	0	0	0	0	0	0	0
16	0	0	0	0	0	0	0	0	0
16.5	0	0	0	0	0	0	0	0	0
17	0	0	0	0	0	0	0	0	0
17.5	0	0	0	0	5	0	0	0	0
18	0	0	0	0	0	0	0	0	0
18.5	0	0	0	0	0	0	0	0	0
19	0	0	0	0	0	0	0	0	0
19.5	0	0	0	0	0	0	0	0	0
20	0	0	0	0	0	0	0	0	0
20.5	0	0	0	0	0	0	0	0	0
21	0	0	0	0	0	0	0	0	0
21.5	0	0	0	0	0	0	0	0	0
22	0	0	0	0	0	0	0	0	0
22.5	0	0	0	0	0	0	0	0	0
23	0	0	0	0	0	0	0	0	0
23.5	0	0	0	0	0	2	0	0	0
24	0	0	0	0	0	0	0	0	0
24.5	0	0	0	0	0	0	0	0	0
25	0	0	0	0	0	3	0	0	0
25.5	0	0	0	0	0	0	0	0	0
26	0	0	0	0	0	0	0	0	0
26.5	0	0	0	0	0	0	0	0	0
27	0	0	0	0	0	0	0	0	0
27.5	0	0	0	0	0	0	0	0	0
28	0	0	0	0	0	0	0	0	0
28.5	0	0	0	0	0	0	0	0	0
29	0	0	0	0	0	0	5	0	0
29.5	0	0	0	0	0	0	0	0	0
30	0	0	0	0	0	0	0	0	0
30.5	0	0	0	0	0	0	0	0	0

Table 10. Buffalo Interchange Combined Phases Stress Range Histogram Data Continued

RANGE	R_AVG	CH_1	CH_2	CH_3	CH_4	CH_5	CH_6	CH_7	CH_8
31	0	0	0	0	0	0	0	0	0
31.5	0	0	0	0	0	0	0	0	0
32	0	0	0	0	0	0	0	0	0
32.5	0	0	0	0	0	0	0	0	0
33	0	0	0	0	0	0	0	0	0
33.5	0	0	0	0	0	0	0	0	0
34	0	0	0	0	0	0	0	0	0
34.5	0	0	0	0	0	0	0	0	0
35	0	0	0	0	0	0	0	0	0
35.5	0	0	0	0	0	0	0	0	0
36	0	0	0	0	0	0	0	0	0
36.5	0	0	0	0	0	0	0	0	0
37	0	0	0	0	0	0	0	0	0
37.5	0	0	0	0	0	0	0	0	0
38	0	0	0	0	0	0	0	0	0
38.5	0	0	0	0	0	0	0	0	0
39	0	0	0	0	0	0	0	0	0
39.5	0	0	0	0	0	0	0	0	0
40	0	0	0	0	0	0	0	0	0
40.5	0	0	0	0	0	0	0	0	0
41	0	0	0	0	0	0	0	0	0
41.5	0	0	0	0	0	0	0	0	0
42	0	0	0	0	0	0	0	0	0
42.5	0	0	0	0	0	0	0	0	0
43	0	0	0	0	0	0	0	0	0
43.5	0	0	0	0	0	0	0	0	0
44	0	0	0	0	0	0	0	0	0
44.5	0	0	0	0	0	0	0	0	0
45	0	0	0	0	0	0	0	0	0
45.5	0	0	0	0	0	0	0	0	0
46	0	0	0	0	0	0	0	0	0
46.5	0	0	0	0	0	0	0	0	0
47	0	0	0	0	0	0	0	0	0
47.5	0	0	0	0	0	0	0	0	0
48	0	0	0	0	0	0	0	0	0
48.5	0	0	0	0	0	0	0	0	0
49	0	0	0	0	0	0	0	0	0
49.5	0	0	0	0	0	0	0	0	0
50	0	0	0	0	0	0	0	0	0
50.5	0	0	0	0	0	0	0	0	0
51	0	0	0	0	0	0	0	0	0
51.5	0	0	0	0	0	0	0	0	0
52	0	0	0	0	0	0	0	0	0
52.5	0	0	0	0	0	0	0	0	0
53	0	0	0	0	0	0	0	0	0
53.5	0	0	0	0	0	0	0	0	0
54	0	0	0	0	0	0	0	0	0
54.5	0	0	0	0	0	0	0	0	0
55	0	0	0	0	0	0	0	0	0
55.5	0	0	0	0	0	0	0	0	0
56	0	0	0	0	0	0	0	0	0
56.5	0	0	0	0	0	0	0	0	0
57	0	0	0	0	0	0	0	0	0
57.5	0	0	0	0	0	0	0	0	0
58	0	0	0	0	0	0	0	0	0
58.5	0	0	0	0	0	0	0	0	0
59	0	0	0	0	0	0	0	0	0
59.5	0	0	0	0	0	0	0	0	0
60	0	0	0	0	0	0	0	0	0
60.5	0	0	0	0	0	0	0	0	0
61	0	0	0	0	0	0	0	0	0
61.5	0	0	0	0	0	0	0	0	0
62	0	0	0	0	0	0	0	0	0

Table 10. Buffalo Interchange Combined Phases Stress Range Histogram Data Continued

RANGE	R_AVG	CH_1	CH_2	CH_3	CH_4	CH_5	CH_6	CH_7	CH_8
62.5	0	0	0	0	0	0	0	0	0
63	0	0	0	0	0	0	0	0	0
63.5	0	0	0	0	0	0	0	0	0
64	0	0	0	0	0	0	0	0	0
64.5	0	0	0	0	0	0	0	0	0
65	0	0	0	0	0	0	0	0	0
65.5	0	0	0	0	0	0	0	0	0
66	0	0	0	0	0	0	0	0	0
66.5	0	0	0	0	0	0	0	0	0
67	0	0	0	0	0	0	0	0	0
67.5	0	0	0	0	0	0	0	0	0
68	0	0	0	0	0	0	0	0	0
68.5	0	0	0	0	0	0	0	0	0
69	0	0	0	0	0	0	0	0	0
69.5	0	0	0	0	0	0	0	0	0
70	0	0	0	0	0	0	0	0	0
70.5	0	0	0	0	0	0	0	0	0
71	0	0	0	0	0	0	0	0	0
71.5	0	0	0	0	0	0	0	0	0
72	0	0	0	0	0	0	0	0	0
72.5	0	0	0	0	0	0	0	0	0
73	0	0	0	0	0	0	0	0	0
73.5	0	0	0	0	0	0	0	0	0
74	0	0	0	0	0	0	0	0	0
74.5	0	0	0	0	0	0	0	0	0
75	0	0	0	0	0	0	0	0	0
75.5	0	0	0	0	0	0	0	0	0
76	0	0	0	0	0	0	0	0	0
76.5	0	0	0	0	0	0	0	0	0
77	0	0	0	0	0	0	0	0	0
77.5	0	0	0	0	0	0	0	0	0
78	0	0	0	0	0	0	0	0	0
78.5	0	0	0	0	0	0	0	0	0
79	0	0	0	0	0	0	0	0	0
79.5	0	0	0	0	0	0	0	0	0
80	0	0	0	0	0	0	0	0	0
S_{reff} (ksi)		**1.52**	**1.50**	**1.58**	**1.61**	**1.53**	**1.49**	**1.58**	**1.60**
% Exceedance		1.78%	1.60%	3.33%	3.79%	1.97%	1.52%	3.32%	3.39%
Remaining Life		>100	>100	>100	>100	>100	>100	>100	>100

Table 11. Dwyer Junction Combined Phases Stress Range Histogram Data

RANGE	R_AVG	CH_1	CH_2	CH_3	CH_4	CH_5	CH_6	CH_7	CH_8
0.25	0	0	0	0	0	0	0	0	0
0.5	58756495	49427823	48623731	52443538	53808486	44144726	53871118	58965834	58756495
1	15800473	11345697	12715045	14407061	13592820	13422877	14124392	16289083	15800473
1.5	3231791	2077159	2321664	2576233	2641484	3012661	2813669	2865717	3231791
2	1278131	1055438	1089362	1217274	1287097	1195015	934662	1336321	1278131
2.5	544908	299076	429889	421841	488814	455321	301945	502197	544908
`3	275615	104326	145310	179323	211918	201695	126590	225810	275615
3.5	133991	44419	64819	80208	94775	92278	56664	104884	133991
4	65275	17895	29291	36133	42557	45911	25913	49718	65275
4.5	32441	7218	13510	17002	18946	23266	12885	24051	32441
5	15706	3551	6042	7729	8722	11711	7640	11842	15706
5.5	7522	1330	2793	3577	4182	7044	3995	5750	7522
6	3798	684	1366	1817	1931	5652	1989	2859	3798
6.5	1819	541	865	779	1184	4271	1023	1311	1819
7	1305	369	459	435	415	2761	772	641	1305
7.5	835	259	228	210	163	2008	588	387	835
8	248	283	61	124	91	1401	408	204	248
8.5	101	258	61	114	59	1219	214	81	101
9	83	265	63	100	24	722	71	55	83
9.5	33	213	38	210	34	426	38	21	33
10	21	205	10	355	23	250	34	21	21
10.5	37	270	20	163	25	239	19	26	37
11	35	231	39	69	26	74	19	21	35
11.5	14	208	13	38	29	94	6	15	14
12	18	170	26	43	24	37	16	26	18
12.5	18	195	18	34	24	34	7	9	18
13	9	112	5	41	7	26	41	18	9
13.5	12	99	17	50	24	30	25	31	12
14	26	59	24	52	24	30	38	44	26
14.5	16	70	23	97	7	39	25	79	16
15	16	63	47	80	17	27	26	49	16
15.5	20	39	20	26	17	27	48	48	20
16	15	40	38	40	8	34	34	30	15
16.5	6	6	6	42	12	6	12	42	6
17	6	6	13	55	6	8	0	30	6
17.5	1	6	11	56	18	8	12	60	1
18	12	6	6	45	18	0	0	72	12
18.5	6	6	6	18	6	6	6	12	6
19	6	6	12	13	18	2	0	6	6
19.5	28	6	6	14	18	14	12	12	28
20	14	12	6	7	6	0	6	6	14
20.5	12	12	6	0	6	12	0	0	12
21	0	6	0	7	24	32	12	0	0
21.5	12	6	12	2	24	20	0	0	12
22	12	18	0	11	78	20	6	0	12
22.5	18	12	6	0	78	2	0	0	18
23	12	18	0	0	48	28	6	0	12
23.5	6	18	6	1	12	18	12	0	6
24	12	54	6	1	24	20	0	0	12
24.5	6	72	6	0	6	8	6	0	6
25	54	60	0	0	42	8	0	0	54
25.5	66	24	6	0	24	6	0	0	66
26	66	36	0	0	24	12	12	0	66
26.5	48	36	6	1	42	0	0	0	48
27	12	18	6	0	42	0	6	0	12
27.5	6	30	6	0	24	12	0	0	6
28	12	12	0	0	6	0	6	10	12
28.5	24	42	6	0	12	6	6	0	24
29	24	90	6	0	0	2	0	0	24
29.5	24	36	6	0	0	6	6	2	24
30	18	24	0	0	0	0	0	1	18
30.5	30	0	18	0	0	6	12	0	30

Table 11. Dwyer Junction Combined Phases Stress Range Histogram Data Continued

RANGE	R_AVG	CH_1	CH_2	CH_3	CH_4	CH_5	CH_6	CH_7	CH_8
31	48	6	6	0	0	8	0	0	48
31.5	36	0	6	0	0	0	0	0	36
32	0	0	6	0	0	0	12	0	0
32.5	6	0	6	0	6	6	0	0	6
33	18	0	6	0	0	6	6	0	18
33.5	0	0	6	0	0	0	0	0	0
34	12	0	0	0	0	0	12	0	12
34.5	0	0	30	0	0	6	0	0	0
35	0	0	24	0	0	6	6	0	0
35.5	0	0	24	0	0	0	0	0	0
36	0	0	12	0	0	8	6	0	0
36.5	0	0	0	0	0	0	6	0	0
37	0	0	0	0	0	0	18	0	0
37.5	0	0	12	0	0	12	18	0	0
38	0	0	12	0	0	8	0	0	0
38.5	0	0	18	0	0	6	12	0	0
39	0	0	6	0	0	0	18	0	0
39.5	0	0	12	0	0	12	0	0	0
40	0	0	6	0	0	12	0	0	0
40.5	0	0	12	0	0	6	6	0	0
41	0	0	6	0	0	12	12	0	0
41.5	0	0	42	0	0	6	36	0	0
42	0	0	24	0	0	6	42	0	0
42.5	0	0	30	0	0	6	30	0	0
43	0	0	12	0	0	6	48	0	0
43.5	0	0	30	0	0	6	12	0	0
44	0	0	6	0	0	6	12	0	0
44.5	0	0	30	0	0	0	6	0	0
45	0	0	12	0	0	12	18	0	0
45.5	0	0	30	0	0	12	12	0	0
46	0	0	36	0	0	24	12	0	0
46.5	0	0	36	0	0	60	18	0	0
47	0	0	18	0	0	42	12	0	0
47.5	0	0	18	0	0	18	12	0	0
48	0	0	18	0	0	18	12	0	0
48.5	0	0	18	0	0	6	18	0	0
49	0	0	12	0	0	6	12	0	0
49.5	0	0	0	0	0	24	24	0	0
50	0	0	0	0	0	24	36	0	0
50.5	0	0	0	0	0	18	30	0	0
51	0	0	0	0	0	6	36	0	0
51.5	0	0	0	0	0	6	12	0	0
52	0	0	0	0	0	6	18	0	0
52.5	0	0	0	0	0	6	12	0	0
53	0	0	0	0	0	12	0	0	0
53.5	0	0	0	0	0	6	0	0	0
54	0	0	0	0	0	12	0	0	0
54.5	0	0	0	0	0	18	0	0	0
55	0	0	0	0	0	36	0	0	0
55.5	0	0	0	0	0	42	0	0	0
56	0	0	0	0	0	24	0	0	0
56.5	0	0	0	0	0	30	0	0	0
57	0	0	0	0	0	12	6	0	0
57.5	0	0	0	0	0	18	0	0	0
58	0	0	0	0	0	6	0	0	0
58.5	0	0	0	0	0	0	0	0	0
59	0	0	0	0	0	0	0	0	0
59.5	0	0	0	0	0	0	0	0	0
60	0	0	0	0	0	0	0	0	0
60.5	0	0	0	0	0	0	0	0	0
61	0	0	0	0	0	0	0	0	0
61.5	0	0	0	0	0	0	0	0	0
62	0	0	0	0	0	0	0	0	0

Table 11. Dwyer Junction Combined Phases Stress Range Histogram Data Continued

RANGE	R_AVG	CH_1	CH_2	CH_3	CH_4	CH_5	CH_6	CH_7	CH_8
62.5	0	0	0	0	0	0	0	0	0
63	0	0	0	0	0	6	0	0	0
63.5	0	0	0	0	0	0	0	0	0
64	0	0	0	0	0	0	0	0	0
64.5	0	0	0	0	0	0	0	0	0
65	0	0	0	0	0	0	0	0	0
65.5	0	0	0	0	0	0	0	0	0
66	0	0	0	0	0	0	0	0	0
66.5	0	0	0	0	0	0	0	0	0
67	0	0	0	0	0	0	0	0	0
67.5	0	0	0	0	0	0	0	0	0
68	0	0	0	0	0	0	0	0	0
68.5	0	0	0	0	0	0	0	0	0
69	0	0	0	0	0	0	0	0	0
69.5	0	0	0	0	0	0	0	0	0
70	0	0	0	0	0	0	0	0	0
70.5	0	0	0	0	0	0	0	0	0
71	0	0	0	0	0	0	0	0	0
71.5	0	0	0	0	0	0	0	0	0
72	0	0	0	0	0	0	0	0	0
72.5	0	0	0	0	0	0	0	0	0
73	0	0	0	0	0	0	0	0	0
73.5	0	0	0	0	0	0	0	0	0
74	0	0	0	0	0	0	0	0	0
74.5	0	0	0	0	0	0	0	0	0
75	0	0	0	0	0	0	0	0	0
75.5	0	0	0	0	0	0	0	0	0
76	0	0	0	0	0	0	0	0	0
76.5	0	0	0	0	0	0	0	0	0
77	0	0	0	0	0	0	0	0	0
77.5	0	0	0	0	0	0	0	0	0
78	0	0	0	0	0	0	0	0	0
78.5	0	0	0	0	0	0	0	0	0
79	0	0	0	0	0	0	0	0	0
79.5	0	0	0	0	0	0	0	0	0
80	0	0	0	0	0	0	0	0	0
S_{reff} (ksi)		**1.75**	**1.72**	**1.75**	**1.74**	**1.76**	**1.72**	**1.67**	**1.76**
% Exceedance		9.63%	5.07%	6.46%	7.24%	8.02%	7.92%	5.57%	8.34%
Remaining Life		36.9	66.4	54.0	48.4	43.3	44.2	60.6	40.7

Table 12. Vedauwoo Interchange Combined Phases Stress Range Histogram Data

RANGE	R_AVG	CH_1	CH_2	CH_3	CH_4	CH_5	CH_6	CH_7	CH_8
0.25	0	0	0	0	0	0	0	0	0
0.5	0.375	137250954	67618350	127662533	129489577	118183988	147200987	134487382	114323268
1	0.75	41874938	23911443	47745291	40659957	36931053	48062191	53914967	40643887
1.5	1.25	10538554	5645708	10458024	8816879	8706611	10418535	10957925	8754730
2	1.75	4530046	2759553	3933072	3193675	3644107	4511805	3907805	2705244
2.5	2.25	1979724	1377307	1508187	1190544	1623920	2266685	1513320	974042
`3	2.75	884582	690646	608999	491461	738493	1095327	598272	373651
3.5	3.25	390663	344064	273446	215936	371474	514335	289439	129547
4	3.75	166857	161260	130808	100506	187387	242490	184755	45148
4.5	4.25	69069	74650	54770	43871	90613	111603	124969	14762
5	4.75	29112	35110	22801	15196	43754	51657	69563	5352
5.5	5.25	12534	15953	9833	5757	17783	23538	30058	1853
6	5.75	5792	8158	4731	2437	8254	12440	11780	638
6.5	6.25	2929	4712	2227	1762	4001	6534	5781	305
7	6.75	1492	2800	1347	1418	2008	3765	2739	160
7.5	7.25	1036	1997	511	1604	1229	2441	1641	68
8	7.75	689	1220	420	1096	718	1572	922	37
8.5	8.25	408	796	272	489	359	1057	646	12
9	8.75	331	587	183	392	195	757	341	0
9.5	9.25	317	425	186	228	76	607	442	0
10	9.75	222	270	182	241	68	399	376	5
10.5	10.25	176	110	247	318	29	235	265	0
11	10.75	64	85	204	329	35	229	143	0
11.5	11.25	43	118	99	155	10	172	113	0
12	11.75	34	64	84	74	30	134	123	0
12.5	12.25	17	96	68	30	20	169	71	0
13	12.75	15	144	66	90	15	192	87	0
13.5	13.25	17	185	28	75	10	116	60	1
14	13.75	27	116	16	69	25	104	56	0
14.5	14.25	17	80	6	70	15	84	19	0
15	14.75	20	68	1	57	20	65	27	0
15.5	15.25	0	64	0	21	0	81	7	0
16	15.75	0	46	0	37	0	41	9	0
16.5	16.25	0	17	2	0	0	36	0	0
17	16.75	4	5	0	0	0	6	1	1
17.5	17.25	2	1	1	0	0	0	0	0
18	17.75	0	1	1	0	0	0	2	0
18.5	18.25	0	0	1	0	0	0	0	0
19	18.75	0	3	3	2	0	0	0	0
19.5	19.25	1	0	1	1	0	0	0	0
20	19.75	0	0	0	3	0	0	1	0
20.5	20.25	1	0	1	1	0	0	0	0
21	20.75	0	1	0	0	0	0	0	0
21.5	21.25	0	0	1	0	0	1	0	0
22	21.75	0	0	1	1	0	0	0	1
22.5	22.25	0	0	1	1	0	0	0	0
23	22.75	1	0	0	0	0	0	0	0
23.5	23.25	0	0	0	0	0	0	0	0
24	23.75	0	0	0	0	0	0	1	0
24.5	24.25	0	1	2	0	0	0	0	0
25	24.75	0	1	2	1	0	0	0	0
25.5	25.25	1	0	0	1	0	0	1	0
26	25.75	0	0	0	0	1	0	1	0
26.5	26.25	1	1	0	1	0	1	0	0
27	26.75	0	0	0	1	0	0	0	0
27.5	27.25	0	0	0	0	0	0	2	2
28	27.75	0	1	0	0	0	0	2	0
28.5	28.25	0	0	0	0	0	0	0	0
29	28.75	0	0	0	0	0	0	2	0
29.5	29.25	0	0	0	0	0	0	2	0
30	29.75	0	0	0	0	0	0	1	0
30.5	30.25	0	0	0	0	0	0	3	0

Table 12. Vedauwoo Interchange Combined Phases Stress Range Histogram Data Continued

RANGE	R_AVG	CH_1	CH_2	CH_3	CH_4	CH_5	CH_6	CH_7	CH_8
31	30.75	0	0	0	0	0	0	0	0
31.5	31.25	0	0	0	0	0	0	11	0
32	31.75	0	0	0	0	0	0	0	0
32.5	32.25	0	0	0	0	0	0	0	0
33	32.75	0	0	0	0	0	0	0	0
33.5	33.25	0	0	0	0	0	0	0	0
34	33.75	0	0	0	0	0	0	0	0
34.5	34.25	0	0	0	0	0	0	0	0
35	34.75	0	0	0	0	0	0	0	0
35.5	35.25	0	0	0	0	0	0	0	0
36	35.75	0	0	0	0	0	0	0	0
36.5	36.25	0	0	0	0	0	0	0	0
37	36.75	0	0	0	0	0	0	0	0
37.5	37.25	0	0	0	0	0	0	0	0
38	37.75	0	0	0	0	0	0	0	0
38.5	38.25	0	0	0	0	0	0	0	0
39	38.75	0	0	0	0	0	0	0	0
39.5	39.25	0	0	0	0	0	0	0	0
40	39.75	0	0	0	0	0	0	0	0
40.5	40.25	0	0	0	0	0	0	0	0
41	40.75	0	0	0	0	0	0	0	0
41.5	41.25	0	0	0	0	0	0	0	0
42	41.75	0	0	0	0	0	0	0	0
42.5	42.25	0	0	0	0	0	0	0	0
43	42.75	0	0	0	0	0	0	0	0
43.5	43.25	0	0	0	0	0	0	0	0
44	43.75	0	0	0	0	0	0	0	0
44.5	44.25	0	0	0	0	0	0	0	0
45	44.75	0	0	0	0	0	0	0	0
45.5	45.25	0	0	0	0	0	0	0	0
46	45.75	0	0	0	0	0	0	0	0
46.5	46.25	0	0	0	0	0	0	0	0
47	46.75	0	0	0	0	0	0	0	0
47.5	47.25	0	0	0	0	0	0	0	0
48	47.75	0	0	0	0	0	0	0	0
48.5	48.25	0	0	0	0	0	0	0	0
49	48.75	0	0	0	0	0	0	0	0
49.5	49.25	0	0	0	0	0	0	0	0
50	49.75	0	0	0	0	0	0	0	0
50.5	50.25	0	0	0	0	0	0	0	0
51	50.75	1	0	0	0	0	0	0	0
51.5	51.25	0	0	0	0	0	0	0	0
52	51.75	0	0	0	0	0	0	0	0
52.5	52.25	0	0	0	0	0	0	0	0
53	52.75	0	0	0	0	0	0	0	0
53.5	53.25	0	0	0	0	0	0	0	0
54	53.75	0	0	0	0	0	0	0	0
54.5	54.25	0	0	0	0	0	0	0	0
55	54.75	0	0	0	0	0	0	0	0
55.5	55.25	0	0	0	0	0	0	0	0
56	55.75	0	0	0	0	0	0	0	0
56.5	56.25	0	0	0	0	0	0	0	0
57	56.75	0	0	0	0	0	0	0	0
57.5	57.25	0	0	0	0	0	0	0	0
58	57.75	0	0	0	0	0	0	0	0
58.5	58.25	0	0	0	0	0	0	0	0
59	58.75	0	0	0	0	0	0	0	0
59.5	59.25	0	0	0	0	0	0	0	0
60	59.75	0	0	0	0	0	0	0	0
60.5	60.25	0	0	0	0	0	0	0	0
61	60.75	0	0	0	0	0	0	0	0
61.5	61.25	0	0	0	0	0	0	0	0
62	61.75	0	0	0	0	0	0	0	0

Table 12. Vedauwoo Interchange Combined Phases Stress Range Histogram Data Continued

RANGE	R_AVG	CH_1	CH_2	CH_3	CH_4	CH_5	CH_6	CH_7	CH_8
62.5	62.25	0	0	0	0	0	0	0	0
63	62.75	0	0	0	0	0	0	0	0
63.5	63.25	0	0	0	0	0	0	0	0
64	63.75	0	0	0	0	0	0	0	0
64.5	64.25	0	0	0	0	0	0	0	0
65	64.75	0	0	0	0	0	0	0	0
65.5	65.25	0	0	0	0	0	0	0	0
66	65.75	0	0	0	0	0	0	0	0
66.5	66.25	0	0	0	0	0	0	0	0
67	66.75	0	0	0	0	0	0	0	0
67.5	67.25	0	0	0	0	0	0	0	0
68	67.75	0	0	0	0	0	0	0	0
68.5	68.25	0	0	0	0	0	0	0	0
69	68.75	0	0	0	0	0	0	0	0
69.5	69.25	0	0	0	0	0	0	0	0
70	69.75	0	0	0	0	0	0	0	0
70.5	70.25	0	0	0	0	0	0	0	0
71	70.75	0	0	0	0	0	0	0	0
71.5	71.25	0	0	0	0	0	0	0	0
72	71.75	0	0	0	0	0	0	0	0
72.5	72.25	0	0	0	0	0	0	0	0
73	72.75	0	0	0	0	0	0	0	0
73.5	73.25	0	0	0	0	0	0	0	0
74	73.75	0	0	0	0	0	0	0	0
74.5	74.25	0	0	0	0	0	0	0	0
75	74.75	0	0	0	0	0	0	0	0
75.5	75.25	0	0	0	0	0	0	0	0
76	75.75	0	0	0	0	0	0	0	0
76.5	76.25	0	0	0	0	0	0	0	0
77	76.75	0	0	0	0	0	0	0	0
77.5	77.25	0	0	0	0	0	0	0	0
78	77.75	0	0	0	0	0	0	0	0
78.5	78.25	0	0	0	0	0	0	0	0
79	78.75	0	0	0	0	0	0	0	0
79.5	79.25	0	0	0	0	0	0	0	0
80	79.75	0	0	0	0	0	0	0	0
S_{reff} (ksi)		**1.77**	**1.82**	**1.71**	**1.70**	**1.76**	**1.80**	**1.70**	**1.67**
% Exceedance		8.42%	12.08%	6.53%	6.27%	9.50%	10.74%	7.47%	4.39%
Remaining Life		-4.5	2.8	-1.7	2.0	-1.5	-5.5	-1.9	5.0